Nano Energy 114 (2023) 108596

Contents lists available at ScienceDirect

Nano Energy

journal homepage: www.elsevier.com/locate/nanoen

Low-grade waste heat recovery scenarios: Pyroelectric, thermomagnetic, and thermogalvanic thermal energy harvesting

Sunghoon Hur [a,b,1], Sangtae Kim [c,1], Hyun-Soo Kim [a], Ajeet Kumar [d], Choah Kwon [c], Joonchul Shin [a], Heemin Kang [e], Tae Hyun Sung [f], Jungho Ryu [d,*], Jeong Min Baik [a,g,h,**], Hyun-Cheol Song [a,g,h,**]

[a] Electronic Materials Research Center, Korea Institute of Science and Technology (KIST), Seoul 02792, Republic of Korea
[b] KHU-KIST Department of Converging Science and Technology, Kyung Hee University, Seoul 02447, Republic of Korea
[c] Department of Nuclear Engineering, Hanyang University, Seoul 04763, Republic of Korea
[d] School of Materials Science & Engineering, Yeungnam University, Gyeongsan 38541, Republic of Korea
[e] Department of Materials Science and Engineering, Korea University, Seoul 02841, Republic of Korea
[f] Department of Electric Engineering, Hanyang University, Seoul 04763, Republic of Korea
[g] School of Advanced Materials Science & Engineering, Sungkyunkwan University, Suwon 16419, Republic of Korea
[h] KIST-SKKU Carbon-Neutral Research Center,Sungkyunkwan University (SKKU), Suwon 16419, Republic of Korea

ARTICLE INFO

Keywords:
Thermal energy harvesting
Pyroelectric
Thermomagnetic
Thermogalvanic
Low grade waste heat

ABSTRACT

Identifying reliable and sustainable sources of electricity is a significant challenge of the present time. However, most energy-generation mechanisms produce unavoidable low-grade waste heat as a byproduct while harvesting (or converting) electrical energy from conventional or renewable energy sources. Each year, over 60% of the primary energy is wasted as heat. Accordingly, considerable efforts are being made to convert this waste heat into usable electrical energy using diverse energy conversion materials. In this review, three actively investigated energy conversion mechanisms beyond thermoelectrics, i.e., (1) pyroelectric, (2) thermomagnetic, and (3) thermogalvanic generators, are reviewed and compared from the viewpoint of fundamental theories, critical parameters for high energy conversion efficiency, and current status of materials and devices. The challenges and opportunities in low-grade waste-heat recovery are discussed in terms of material science and structural design. This review provides an overview of the current progress in thermal-energy-harvesting research, future challenges, and opportunities.

1. Introduction

In line with the Paris Agreement, the world has to establish global net-zero emissions by 2050 to limit global warming to 1.5 °C [1,2]. However, global energy use has steadily increased over the last few decades, and this growing energy demand trend is expected to continue over the next decade (Fig. 1) [3]. To achieve both net-zero carbon emissions and increasing energy demand, two fields of study must be conducted in parallel: renewable energy and energy conversion efficiency. Renewable energy sources, such as wind and solar power, have been actively investigated, and their share has been increasing, reaching above 10% of the global power mix [4].

In addition to renewables, increasing energy conversion efficiency is pivotal to achieving zero-carbon emissions and global sustainability. Recently, the International Energy Agency (IEA) reported that ~624 EJ (exajoule or 10^{18} joule) of energy was supplied globally in 2021, which is equivalent to 14,901 million tonnes of oil equivalent (Mtoe). It is also reported that over 60% of the energy provided is wasted as heat. In other words, two-thirds of the globally consumed energy is lost during energy conversion, and most of it is released as heat [6–8]. This significant wastage should be re-examined because only one-third of the global energy supply is used for services. Therefore, improving energy conversion efficiency by focusing on waste-heat recovery is crucial in addressing global zero-carbon commitments, mitigating climate change,

* Corresponding author.
** Corresponding authors at: Electronic Materials Research Center, Korea Institute of Science and Technology (KIST), Seoul 02792, Republic of Korea.
E-mail addresses: jhryu@ynu.ac.kr (J. Ryu), jbaik@skku.edu (J.M. Baik), hcsong@kist.re.kr (H.-C. Song).
[1] S.H., and S.K. contributed equally to this work.

https://doi.org/10.1016/j.nanoen.2023.108596
Received 22 February 2023; Received in revised form 22 May 2023; Accepted 6 June 2023
Available online 14 June 2023

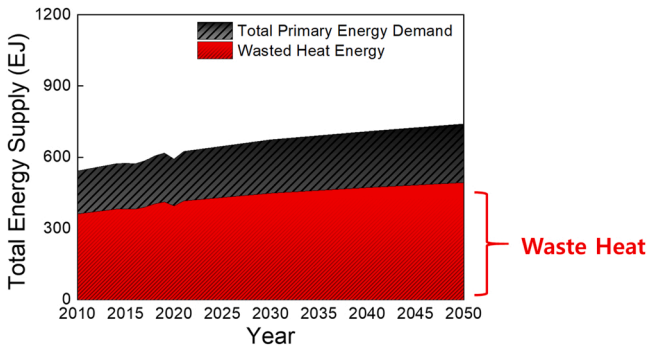

Fig. 1. Global primary energy demand trends projected to the year 2050 and the portion of waste heat in total energy use [3,5].

and meeting future energy demands.

Waste heat is a form of energy that is not utilized for practical purposes and is released into the environment. Owing to the second law of thermodynamics, which states that the energy conversion efficiency cannot be 100%, waste heat is generated in every energy conversion process used in various industrial systems [9]. The most significant waste heat source is exhaust air from heating systems, such as burners, furnaces, dryers, and heat exchangers [10]. If we evaluate waste heat in detail, it is classified into three grades: high temperature (above 650 °C), medium temperature (230–650 °C), and low temperature (below 230 °C) [11]. High- and medium-grade waste heat may be effectively recaptured and recovered because it is often congregated and present near power plants. In addition, the thermal cycle efficiency, determined by the temperature difference between the heat source and sink, is lucrative at high temperatures; therefore, several techniques have been developed and operated in medium- and high-temperature ranges [12].

Consequently, most existing power plants and marine vessels are equipped with waste-heat recovery systems to increase fuel efficiency [13,14]. In the case of low-grade (below 230 °C) waste heat, however, it is often neglected owing to its ineffective conversion merits and difficulties in being recaptured because the heat source is more pervasive and less concentrated than higher-temperature waste heat [10]. Moreover, the low-grade waste-heat recovery process cannot achieve an efficiency comparable to those of medium- and high-grade waste-heat recovery processes.

Despite the poor qualities and inefficiencies of low-grade waste-heat recovery, it should be explored further because of its high amount of potential recoverable energy, which exceeds that of medium- and high-grade waste heat combined (Fig. 2) [11]. Accordingly, waste heat energy, particularly low-grade heat, can be a key research area to satisfy the increasing energy demand and lower carbon emissions [15,16].

A practical method for recovering low-grade waste heat to generate electricity can revolutionize global energy demand issues. In the last few decades, many efforts have been made to recapture the waste heat [18–20]. A heat pump is a viable option that can be operated on a large scale, but its usage is mainly focused on building heating rather than electricity generation [21,22]. In addition, the necessity of fluids for heat exchange limits its miniaturization, and exhaust gases and liquids can cause safety issues [15].

On the other hand, solid-state devices can be freely installed in any location, requiring minimal operational costs and space to recapture the available thermal energy [20]. Furthermore, low-grade waste heat is often widespread and located near end-use sites. Accordingly, solid-state thermal energy harvesters are more effective in low-grade waste-heat recovery because they can be placed in proximity to heat sources owing to their compactness, quietness, and robustness. Most solid-state thermal-energy-harvesting device mechanisms are rooted in various technologies, including thermoelectric, pyroelectric, thermomagnetic, and thermionic technology. [18–20,23–25].

Thermoelectric (TE) technology is typically used to recover waste heat [16,18,19,25,26]. Since the discovery of bismuth telluride (Bi_2Te_3) in the late 1950 s, thermoelectric materials have been actively investigated. The thermoelectric performance of a given material can be evaluated using a dimensionless figure of merit (ZT), which is defined as follows:

$$ZT = \frac{\alpha^2 \sigma}{k} T \tag{1}$$

where α is the Seebeck coefficient, σ is the electrical conductivity, k is the thermal conductivity, and T is the absolute temperature in Kelvin [27]. A higher ZT value implies a higher thermoelectric effect, which is linearly proportional to temperature (T). Therefore, thermoelectric generator systems for waste-heat recovery are preferable at higher temperature differences between the cold and hot sides. Moreover, it is difficult to maintain a temperature gradient of more than 5 °C between the cold and hot sides because of thermal equilibrium within the solid. For this reason, thermoelectric low-waste-heat recovery research was not summarized in this review.

In addition to thermoelectric methods, the thermoelastic method is excluded from this review because it provides relatively insufficient power density compared to other mechanisms [20]. Consequently, this paper reviews three mechanisms for harvesting low-grade waste heat: pyroelectric, thermomagnetic, and thermogalvanic mechanisms. The pyroelectric and thermomagnetic mechanisms have been widely studied, and a significant amount of research has been conducted. On the other hand, the thermogalvanic approach, a subdivision of thermoionic approaches, is a comparatively new approach for thermal energy harvesting. In Fig. 3, the number of papers published on these approaches have increased in recent years.

2. Pyroelectric

2.1. Fundamental principles of pyroelectricity

Pyroelectrics can harvest energy in an environment where the temperature is spatially uniform without a gradient, but spontaneous polarization in certain non-centrosymmetric solids changes with time-dependent temperature variation [28]. The origin of pyroelectricity in pyroelectric materials is the polarization response to temperature

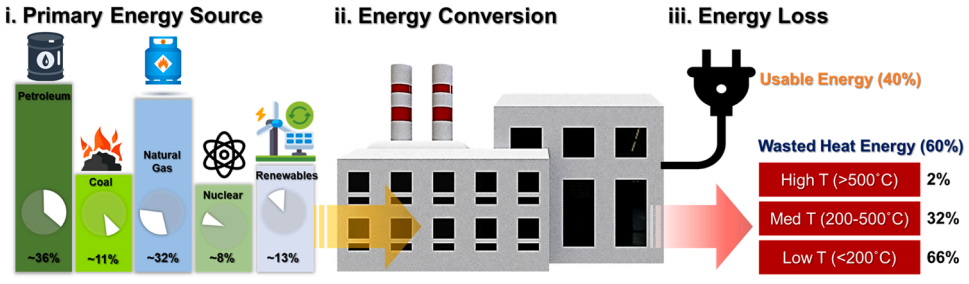

Fig. 2. Schematics of supplied energy flow and share of waste heat in temperature ranges [6,15,17].

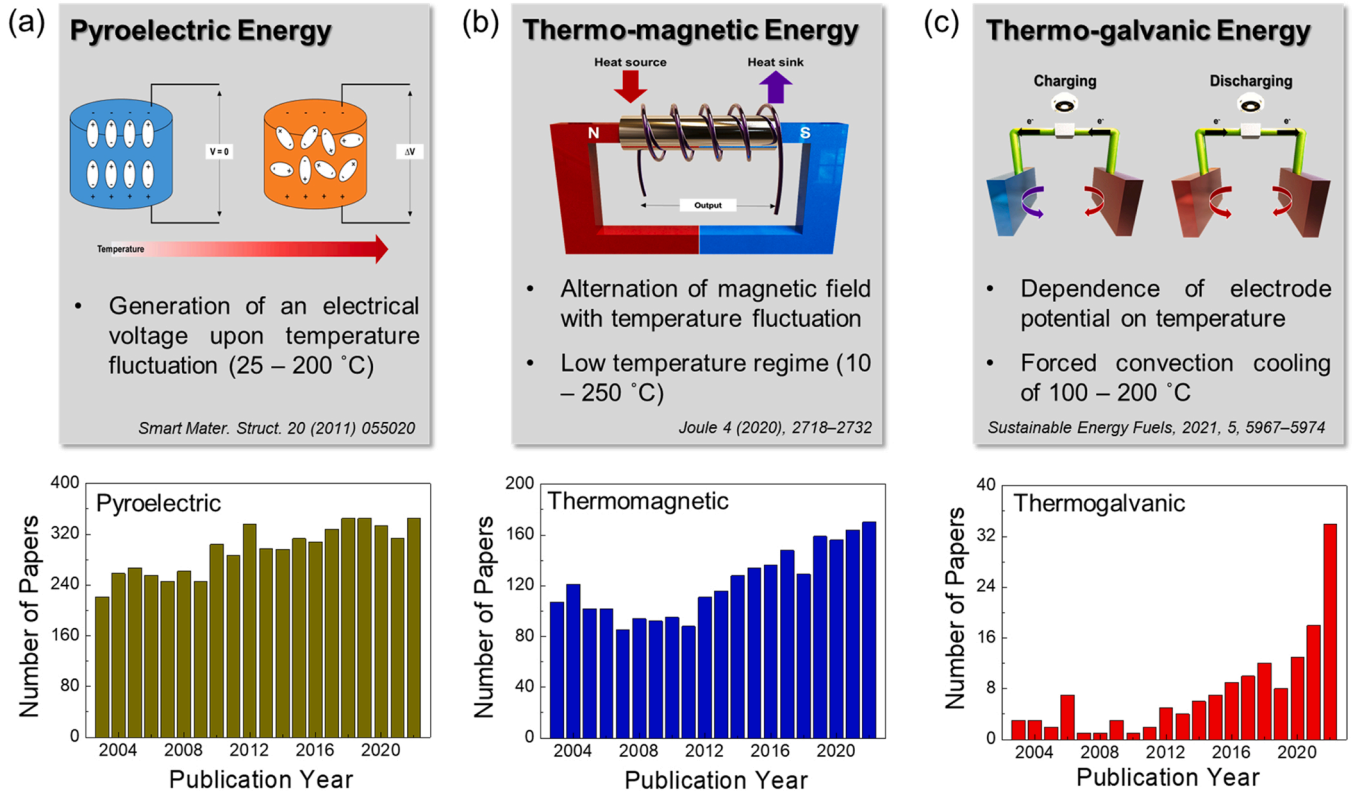

Fig. 3. Number of papers published in the (a) pyroelectric, (b) thermomagnetic, and (c) thermogalvanic fields from the year 2003–2022. These numbers were obtained by searching "pyroelectric," "thermomagnetic," and "thermogalvanic" in the tile of the articles on SCOPUS.

fluctuations [29]. Among the various pyroelectric materials for thermal-energy-harvesting applications, ferroelectric-based pyroelectric materials exhibit high performance owing to their sizeable spontaneous polarization (P_s). Ferroelectric materials possess temperature-dependent P_s along a unique crystallographic direction. They can generate a charge flow, i.e., an electric current with a change in the temperature (both in the heating or cooling process) due to small changes in their ionic positions. Both pyro- and ferroelectric materials (a subgroup of piezoelectric materials) must be non-centrosymmetric and polar. In Fig. 4, Regions I and II show the response of the pyroelectric material to thermal fluctuations in tetragonal (polar/ferroelectric) and cubic (non-polar/paraelectric) structures, respectively. The pyroelectric coefficient (p) increases with temperature due to the increased dipole and domain motion, achieving a maximum when $T \approx T_c$ is in Region III.

2.2. Pyroelectric coefficient, figure of merits (FoMs), and characterization

When a pyroelectric capacitive structure with a temporal temperature gradient is connected to an external circuit, the generation of a surface charge induces a pyroelectric current (I_p). The pyroelectric coefficient (p) is given by the following:

$$p = \frac{I_p}{\frac{dQ}{dt}} = \frac{I_p}{A\frac{dT}{dt}} \tag{2}$$

where A is the effective area of the capacitor and Q is the generated pyroelectric charge [31].

Several material figure-of-merit (FoMs) have been used as criteria for selecting the proper pyroelectric materials for various applications. The pyroelectric material with high current (F_i), voltage (F_v), and detectivity (F_D) are shown by the following:

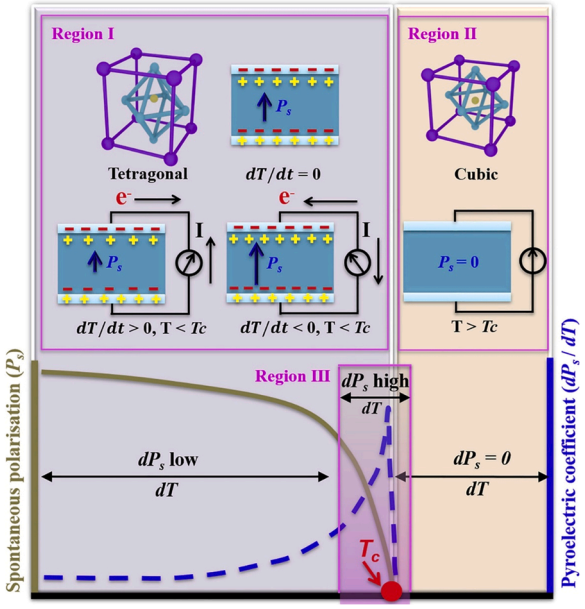

Fig. 4. Schematic of the pyroelectric material response in (a) Region-I, $T < Tc$, (b) Region-II, $T > T_c$, and (c) condition for high pyroelectric response [30]. Copyright 2020. *Cell Press.*

$$F_i = \frac{p}{C_E} = \frac{p}{\rho C_P} \tag{3}$$

$$F_v = \frac{p}{C_E \varepsilon_{33}^{\sigma}} = \frac{p}{\rho C_P \varepsilon_{33}^{\sigma}} \tag{4}$$

$$F_D = \frac{p}{C_E\sqrt{\varepsilon_{33}^{\sigma}\tan\delta}} = \frac{p}{\rho C_P\sqrt{\varepsilon_{33}^{\sigma}\tan\delta}} \quad (5)$$

where c_E and c_P are the volume-specific heat (J/m^{3}K) and specific heat capacity (J/kg·K), respectively. The density of the material is given by ρ (kg/m^3), $\varepsilon_{33}^{\sigma}$ is the dielectric permittivity in the polarization direction at constant stress σ, *and* $\tan\delta$ is the dielectric loss. In the case of pyroelectric energy harvester, the electro-thermal coupling factor (k^2) and F_E should be considered, which are shown by the following:

$$k^2 = \frac{p^2 T_{hot}}{C_E \varepsilon_{33}^{\sigma}} = \frac{p^2 T_{hot}}{\rho C_P \varepsilon_{33}^{\sigma}} \quad (6)$$

$$F_E = \frac{p^2}{\varepsilon_{33}^{\sigma}} \quad (7)$$

where T_{hot} is the maximum operating temperature [31–33].

Because FoMs are directly related to p, quantifiable determination of p is critical. To determine p, three methods (static, indirect, and dynamic) can be used depending on the temperature stimulus and measured parameter [34]. In the static method, p is calculated by the difference in pyroelectric charges, measured at discrete temperatures. However, this method is prone to inducing charge compensation from conduction through air or leakage current through the sample. Indirect methods measure p via polarization measurement, but these methods may be susceptible to incomplete polarization switching or fatigue [35]. In dynamic methods, the Byer-Roundy technique [36] involves a continuous temperature change, and the Chynoweth method [37] periodically oscillates the temperature. Because the pyroelectric effect is reversible, the pyroelectric current generated from heating should be equal but opposite to that generated from cooling. Oscillating the temperature enables the separation of the actual pyroelectric current response to improve accuracy. In this sense, the Chynoweth dynamic method is the most reliable and widely used method for measuring p, as shown in Fig. 5.

2.3. High-performance pyroelectric materials for thermal energy harvesting

Perovskite ceramics are generally robust and insensitive to moisture and vacuum, with a high p and low loss. The pyroelectric properties of perovskite ceramics strongly depend on their composition. Large pyroelectric FoMs were found for the $Ba_{0.85}Sr_{0.15}Zr_{0.1}Ti_{0.9}O_3$ composition with a current responsivity (F_i) of 600 pm/V at 303 K [39]. Introducing doping into materials is also considered the easiest way to alter or tune electrical properties. The pyroelectric properties were enhanced in Mn-doped lead zirconate titanate (PMZT) thin films with excellent ferroelectric (no hysteretic fatigue) and retention properties owing to reduced oxygen vacancy mobility. Mn^{4+} ions are formed by consuming the oxygen vacancies generated during repeated switching in Mn^{2+} ions. Moreover, Mn-doping leads to a significant reduction in dielectric constant (~31%) and loss (~96%), which results in a significant improvement in the p (~67%) and ~3 times improvement in the pyroelectric detectivity figures of merit (F_d) (~235%) [40]. In the case of relaxor-$PbTiO_3$ single crystals such as $Pb(Mg_{1/3}Nb_{2/3})O_3$-$PbTiO_3$, it is also known that the pyroelectricity and FoM can be significantly enhanced by Mn doping for the same reason [41]. A giant pyroelectric figure of merit has also been reported for La and Ta co-doped lead-free $0.94Na_{0.5}Bi_{0.5}TiO_3$–$0.06BaTiO_3$ ceramics with F_i = 461 pm/V, F_v = 0.078 m^2/C, and F_d = 2.76 μPa$^{-1/2}$ [42]. The enhancement in the low-grade waste heat recovery by lead-free $BaZrTiO_3$ ceramics is reported by Ngo et al. [43] by doping Sr and Ca isovalent dopants. The smaller ionic radii of the isovalent dopants Sr and Ca improved the relaxor behavior, hence enhanced the pyroelectric conversion ability of $Ba(Zr_{0.1}Ti_{0.9})O_3$ ceramics.

A considerable value of p can also be found in materials with the coexistence of multiple phases in a particular temperature range. Hence, the pyroelectric properties can be improved if a material is engineered to possess two phases or a multiphase close to room temperature with a low energy barrier of polarization rotation [44]. For Pb $[(Mn_xNb_{1-x})_{1/2}(Mn_xSb_{1-x})_{1/2}]_y(Zr_zTi_{1-z})_{1-y}O_3$ (PMN-PMS-PZT) ceramics, for example, three different Zr/Ti compositions of 95/5 (Zr95), 85/15 (Zr85), and (Zr85 + Zr95) were prepared because the Zr/Ti ratio affected the phases of the ceramics. The p value of the Zr95 ceramic was ~6000 μC/m^{2}K, which was more than 2–3 times higher than that of other reported pyroelectric ceramics. The output power was 25.7 μW, 4.8 μW, and 14.2 μW at a composition ratio of Zr95, Zr85, and (Zr85 + Zr95), respectively, under identical conditions [45].

An enhanced pyroelectric response was also achieved via domain engineering from [001] grain-oriented, tetragonal-phase, lead-free 0.2 (2/3 $K_{0.5}Bi_{0.5}TiO_3$-1/3$BaTiO_3$)− 0.8$Na_{0.5}Bi_{0.5}TiO_3$ (KBT-BT-NBT) ceramics prepared by the templated grain growth method, as shown in Fig. 6 [46]. The textured KBT-BT-NBT ceramics show significant enhancements in the FoM values F_i ~206 pm/V, F_v ~0.035 m^2/C, and F_d ~16.4 μPa$^{-1/2}$ with pyroelectric coefficients of p_{TSDC} ~326 μC/m^{2}K at room temperature and p_{TSDC} ~90,900 μC/m^{2}K at depolarization temperature (T_d).Tables 1–3.

The dimensionality effect on pyroelectricity in three types of materials, van der Waals (vdW) (In_2Se_3), quasi-vdW ($CsBiNb_2O_7$), and ionic/covalent (ZnO) materials, was investigated by Jiang et al. [29]. It was

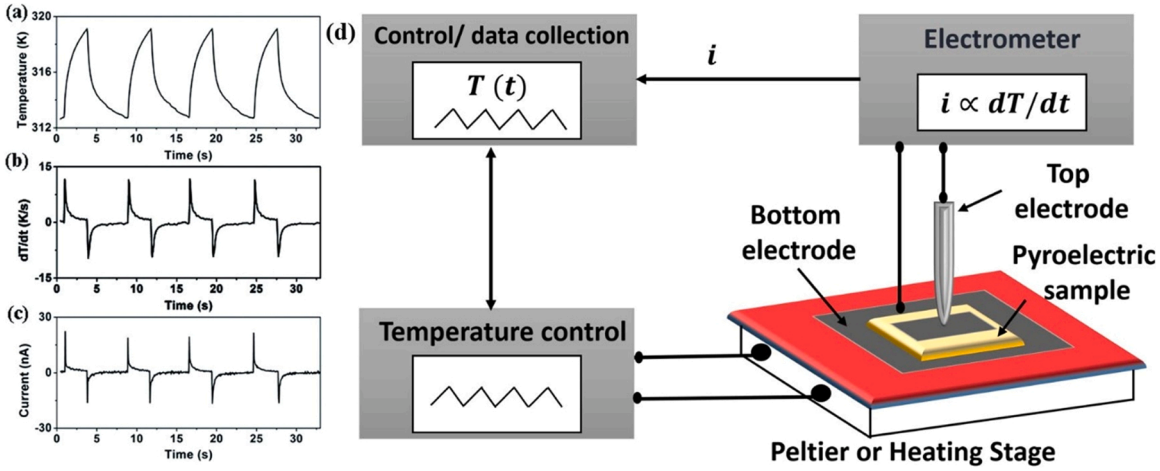

Fig. 5. Change in (a) temperature, (b) dT/dt, and (c) output current vs. time plots [38]. (d) Schematic of the measurement set-up for the pyroelectric measurement. Copyright 2018. *Royal Chemical Society*.

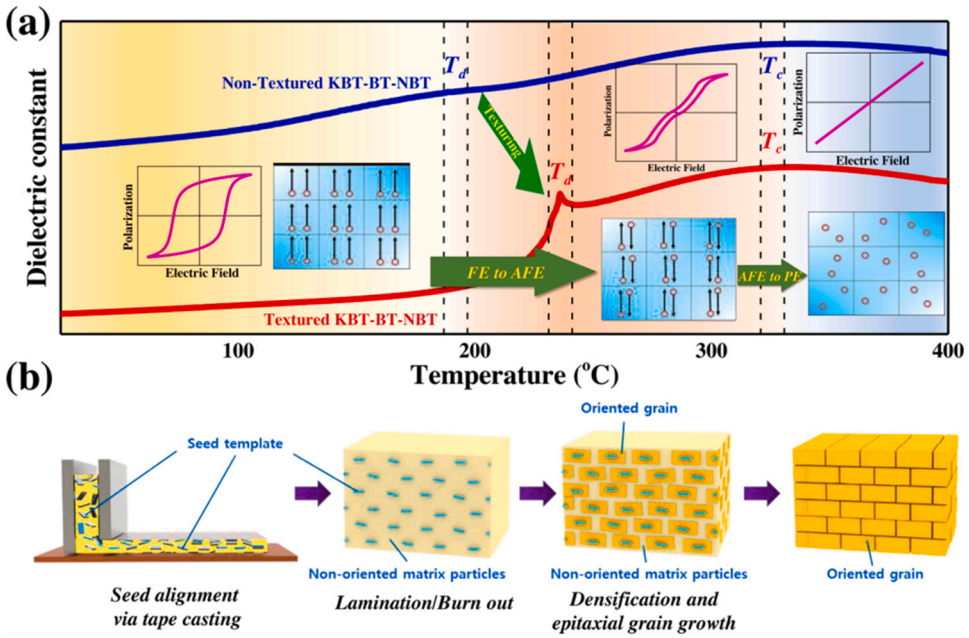

Fig. 6. (a) Schematic illustration of the texture-driven sharp ferroelectric to antiferroelectric phase transition in the KBT-BT-NBT ceramic with p near the transition temperature. (b) Schematics of the synthesis mechanism of the [001] oriented KBT-BT-NBT ceramic [46]. Copyright 2021. *Elsevier*.

Table 1
Comparison of the developed materials' pyroelectric performance. p: pyroelectric coefficient, T_d or T_c: Depolarization or Curie temperature, F_D ($\mu Pa^{-0.5}$): figures of merit for voltage responsibility, F_v (m^2/C): figures of merit for detectivity, F_i (pm/V): figures of merit for current responsivity, PFA: Pore-forming agent, CNT: Carbon nanotubes, PMMA: poly (methyl methacrylate)).

Ref.	Year	Material	Type	P ($\mu C/m^2K$)	Temperature (T_d or T_c) (K)	FOMs (F_D, F_v, or F_i)
S. Jiang et al.[47]	2015	$Ba_{0.67}Sr_{0.33}TiO_3$ (BST)	Lead-free	5500	295 (T_c)	12.5 (F_D)
S. Jiang et al.[47]	2015	$Ba_{0.67}Sr_{0.33}TiO_3$ (BST)	Lead-free: PFA: PMMA	8000	297 (T_c)	27.5 (F_D)
S. Jiang et al.[47]	2015	$Ba_{0.67}Sr_{0.33}TiO_3$ (BST)	Lead-free: PFA: CNT	9500	299 (T_c)	32 (F_D)
H. Zhang et al.[48]	2010	$Bi_{0.5}(Na_{0.82}K_{0.18})_{0.5}TiO_3$ (Thick films)	Lead-free: PFA: Ethyl cellulose	420	-	38 (F_D)
K. S. Srikanth et al.[49]	2017	$BaSn_{0.05}Ti_{0.95}O_3$(2% PMMA)	Lead-free: PFA: 2% PMMA	557	355 (T_c)	12 (F_D), 0.018 (F_v), 228 (F_i)
Q. Zhang et al.[40]	2003	$Pb(Zr_{0.3}Ti_{0.7})O_3$)	Lead-based 1%Mn doped	352	-	38.5 (F_D)
R. Sun et al.[50]	2014	$Mn{:}94.6Na_{0.5}Bi_{0.5}TiO_3 - 5.4BaTiO_3$ [001]	Lead-free Mn-doped Single crystal	380	553(T_c)	29.8 (F_D), 0.082 (F_v), 131 (F_i)
S. B. Lang et al.[51]	2001	PVDF	Polymer	27	383 (T_c)	0.147 (F_v), 100 (F_i)
S. B. Lang et al.[51]	2001	Triglycine sulphate $(NH_2CH_2COOH)_3H_2SO_4$	Single crystal Sulphate	280	322 (T_c)	0.362 (F_v), 121 (F_i)
K. S. Srikanth et al.[44]	2018	$(Ba,Ca)TiO_3$-$xBa(Sn,Ti)O_3$	Lead-free	205	325(x = 0.6) ~ 395(x = 0) (T_c)	9.8 (F_D)
A. M. Balakt et al.[42]	2017	0.005La-NBT-0.06BT-0.002Ta at RT	Lead-free	1292	313 (T_d)	2.8 (F_D), 0.078 (F_v), 461 (F_i)
A. M. Balakt et al.[42]	2017	0.002La-NBT-0.06BT-0.002Ta at T_d (61.3 °C)	Lead-free	5862	318 (T_d),	7.6 (F_D), 0.18 (F_v), 2094 (F_i)
N. C. T. Ngo et al.[43]	2023	Sr and Ca doped $Ba(Zr_{0.1}Ti_{0.9})O_3$	Lead free		383–388 (T_c)	
L. Hu et al.[52]	2023	BNT-xBNN	Lead free	7910	423 (T_d)	21.05 (F_D), 0.05 (F_v), 277 (F_i)
X. Lei et al.[53]	2012	Lead strontium titanate (PST) ceramics	Lead-based	6000	301 (T_c)	
J. A. Gallagher et al.[54]	2014	PIN-PMN-PT	Single crystal	650	-	
F. A. He et al.[55]	2016	(PVDF) composite	Polymer	2670	-	
A. Hussain et al.[56]	2016	$0.75Pb(Mg_{1/3}$-$Nb_{2/3})O_3$-$0.25PbTiO_3$	ceramics	2739	483 (T_c)	
T. Yu et al.[57]	2015	PMnN-PMS-PZT	Lead-free	2650	301 (Zr_{95}) ~ 316 (Zr_{96}) (T_d)	
J. Jiang et al.[29]	2022	In_2Se_3	Lead-free, Thin film (11 nm)	5500		24.2 (F_v)
J. Jiang et al.[29]	2022	ZnO	Lead-free, Thin film (32 nm)	8700		32.6 (F_v),

found that thin sheets showed a large p than thick sheets. This is attributed to the possible reduced thickness influence of the changed phonon dynamics in the crystals on their pyroelectricity. In other words, atomic displacements related electron-phonon renormalization contributes to pyroelectricity. As the crystal's thickness decreased, there were fewer restrictions for atoms to be displaced. In a 3D system, atomic displacements are restrained by atoms in all directions. On the other hand, in a 2D system, because such constriction is absent, atomic

Table 2
Comparison of the thermomagnetic generator performance according to the harvesting method.

Ref.	Year	Harvesting method	Magnet material	Temp (K)	Freq (Hz).	Power (mW)
X. Liu et al.[96]	2023	Induction coil	Gd	288 ~ 353	1 ~ 12	
A. Waske et al.[97]	2019	Induction coil	Nd-Fe-B & La-Fe-Co-Si	285 ~ 315	1	1.24
Z. Ma et al.[99]	2021	Induction coil	$La(Fe, Si)_{13}H_y$/In	340	0.02	1×10^{-4}
R. A. Kishore et al.[101]	2019	Axial flux electric generator	Gd & Nd	313	12.7 ~ 14.3	1.3
J. Chun et al.[102]	2017	Piezoelectric	Gd & Nd	343	1 ~ 3	0.158
H. C. Song et al.[103]	2017	Piezoelectric	$(Ni_{0.6}Cu_{0.2}Zn_{0.2})Fe_2O_4$	353	0.2	0.017
M. Ujihara et al.[93]	2007	Piezoelectric	Gd & NdFeB	323	28	1.3×10^{-6}
J. Chun et al.[104]	2018	Piezoelectric	Gd & Nd	323	9	0.08
R. Ahmed et al.[105]	2019	Triboelectric	Gd	296	4.4	14.4×10^{-3}
C. Rodrigues et al.[106]	2022	Triboelectric	Gd & NdFeB	338	11×10^{-3}	358
X. Cao et al.[107]	2022	Triboelectric	Ni	373	1	4.45

Table 3
Notable thermogalvanic electrode materials according to the mechanisms and phases.

Ref.	Year	Working Principle	Electrode material (Phase)	Temp. Ranges (K)	Thermopower (mV/K)
M.J. Schmid et al.[113]	2015	Thermo-galvanic	Li (solid)	300–340	1.7
N.P. Yao et al.[114]	1971	Thermo-galvanic	Li-Al (solid)	300–340	1.5
Y. Reynier et al.[115]	2004	Thermo-galvanic	$LiCoO_2$ (solid)	300–340	1.2
J.P. Pereiraramos et al.[116]	1988	Thermo-galvanic	$Li_xV_2O_5$ (solid)	300–340	2.1
M. Bonetti et al.[117]	2011	Soret	tetrabutylammonium nitrate (liquid)	303–318	7.0
J. Duan et al.[119]	2018	Thermo-galvanic	$Fe[CN]_6]^{3-/4-}$ + guanidinium (liquid)	293–323	4.2
B. Yu et al.[120]	2020	Thermo-galvanic	$Fe[CN]_6]^{3-/4-}$ + guanidinium cation (liquid)	293–333	3.7
C.-G. Han et al.[122]	2020	Thermo-galvanic + Soret	$Fe[CN]_6]^{3-/4-}$ + gelatin + KCl (liquid)	293–301.5	17.0
Y. Han et al.[121]	2022	Thermo-galvanic	KCl + methylcellulose + I^-/I_3^- (liquid)	297–358	9.62 / 8.18
D. Zhang et al.[125]	2022	Thermo-galvanic	$Fe[CN]_6]^{3-/4-}$ + guanidinium	298–338	4.4

displacements become more prominent, and they show pyroelectric properties very different from those of a 3D system. It also exhibited the greatest dimensionality effect, with chemical bonds along the out-of-plane direction. As a result, ionic/covalent ZnO showed the highest enhancement in pyroelectric properties [29].

2.4. Thermal-energy-harvesting device with pyroelectricity

At a small scale, pyroelectric devices (temporal temperature gradient, dT/dt, where T is the temperature and t is the time) are better suited for thermal-to-electrical energy conversion than thermoelectric devices (spatial temperature gradient dT/dx, where x is the distance). Pyroelectric energy conversion from low-grade waste heat energy, induced by temperature- and field-induced polarization susceptibilities, is sufficient to power wireless sensors, medical diagnostics, and other microelectronics [8,23,58–60]. More importantly, pyeoelectric energy havester (PyEH) does not require moving parts and requires minimal maintenance.

To extract electrical work from waste heat, pyroelectric energy conversion requires thermodynamic cycles, which is the opposite of the steady-state operation of thermoelectrics. These cycles include the Stirling cycle with two isothermal and two iso-displacement processes [61,62], the Carnot cycle with two isothermal and two adiabatic processes [63], the Ericsson cycle, and the Olsen cycle [64], which includes two isothermal and two isoelectric processes [64–69]. Fig. 7(a) and (b) show schematics of the pyroelectric Ericsson cycle with isothermal and isoelectric processes. As reported, adapted Ericsson cycles are claimed to extract the maximum potential work from a pyroelectric cycle out of all thermodynamic cycles [8,70]. An example of the use of the pyroelectric Olsen cycle for thermal energy harvesting was recently published by Lheritier et al. [23] in which the entropy (S)–temperature (T) diagram of a nonlinear pyroelectric (NLP) of lead scandium tantalite (PST) shows an electric-field-driven ferroelectric–paraelectric phase transition. Fig. 7(c) shows the experimental isothermal hysteresis curves for a vinylidene fluoride–trifluoroethylene (VDF-TrFE) co-polymer containing 56 mol% VDF (56/44 P(VDF-TrFE)) at different temperatures, highlighting the strong temperature dependence of the co-polymer polarization. The thermodynamic cycle shown in Fig. 7(c) can be used for thermal energy harvesting by utilizing the polarization difference between the two temperatures, referred to as the Ericsson cycle [71]. Similarly, the Olsen cycle was also performed on co-polymer 60/40 [P(VDF-TrFE)] thin films sandwiched between metallic electrodes, as shown in Fig. 7(d). The Olsen cycle's low and high electric fields are 202 and 379 kV/cm, respectively. As a result, an energy density of 130 mJ/cm^3 was achieved at 0.061 Hz frequency with temperature oscillating between 69.3 °C and 87.6 °C. Furthermore, a power density of 10.7 mW/cm^3 at 0.12 Hz was reported between 70.5 and 85.3 °C. [72]. Recently, using Niobium-doped lead zirconate titanate stannate (PNZST) ceramics as pyroelectric materials, the maximum power density was reported as 149 mW/cm^3 over a temperature range of 150–220 °C and an electric field of 13 kV/cm [73].

Fig. 8(a) shows a schematic of the Ericsson-based pyroelectric thermal-electrical energy conversion test setup consisting of a $BaTiO_3$ thin-film capacitor with electrodes. A gold strip placed above the pyroelectric capacitor served as a resistive heater. A SiO_2 layer sandwiched between the top electrode and heater strip electrically insulates the pyroelectric film and minimizes heating voltage interference [75]. Cha et al. [1] experimentally demonstrated the feasibility of pyroelectric energy harvesters that use liquid-based thermal interfaces for the rapid switching of the thermal conductance between a pyroelectric material and a heat source, thereby delivering a high output power density (Fig. 8 (b)). Pyroelectric thermal energy harvesting consists of a pyroelectric co-polymer thin film with a mechanical actuator harvested at power densities as high as 110 mW/cm^3 at frequencies of ~1 Hz. The colossal energy-harvesting capabilities of antiferroelectric $Hf_xZr_{1-x}O_2$ (HZO, $x = 0.1$–0.3) film-based pyroelectric energy harvesters were reported by Park et al. [76]. $Hf_{0.2}Zr_{0.8}O_2$ and $Hf_{0.3}Zr_{0.7}O_2$ films were tested as pyroelectric energy harvesters with the harvested energy densities of 11.5

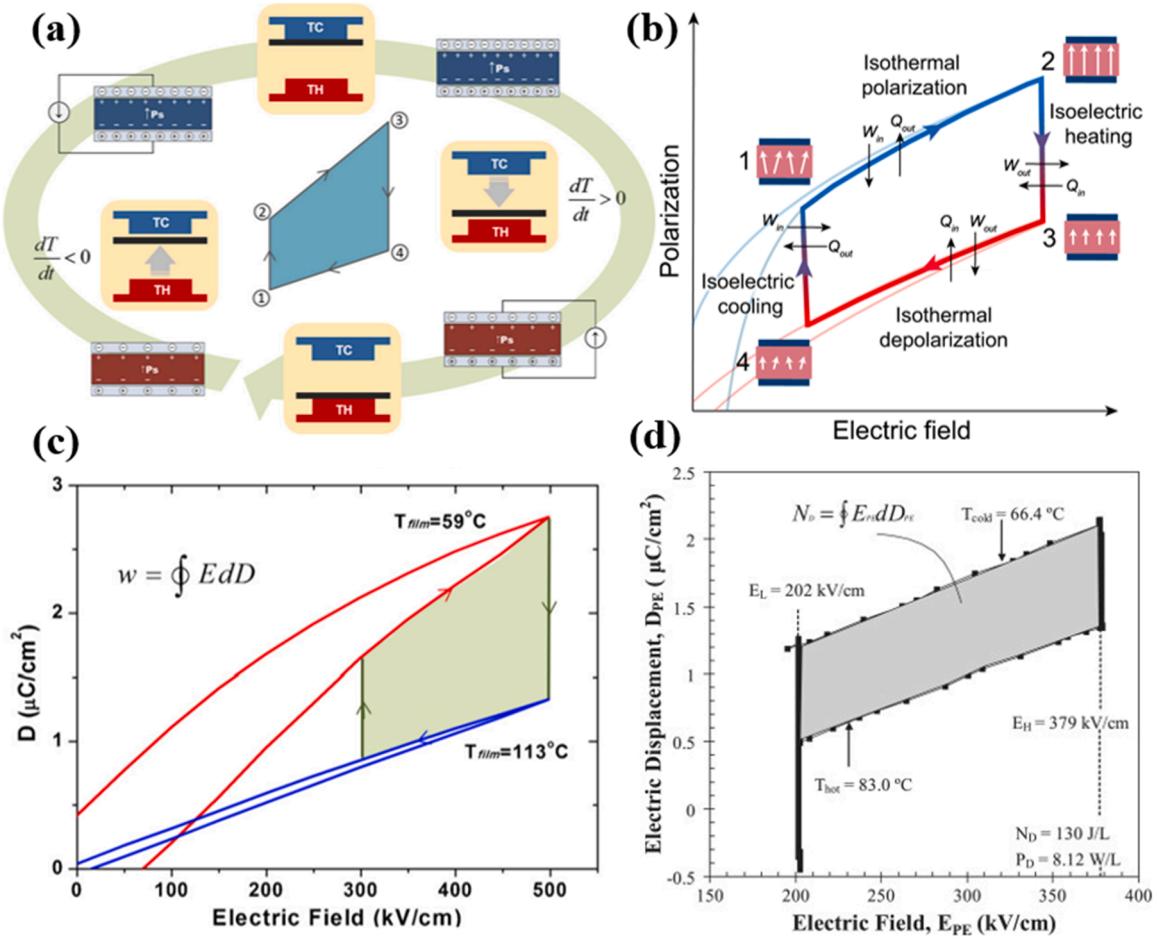

Fig. 7. Schematics of (a) Ericsson pyroelectric thermal-to-electric conversion cycle within each state during a device operation [71] Copyright 2013. Elsevier, and (b) polarization vs. electric-field pathways for Ericsson (Olsen) cycles [74]. Copyright 2019. *Nature Publishing Group* (c) Example of isothermal hysteresis curves based on the Ericsson cycle. A shaded area corresponds to the harvestable energy that excludes the hysteresis loss [71]. (d) Electric displacement versus electric field (*D-E*) for a 1 cm^2 pyroelectric element with 45.7 μm thickness [72]. Copyright 2010. *Elsevier*.

and 5.7 J/cm^3 in each Olsen cycle. $Hf_xZr_{1-x}O_2$ (HZO, $x = 0.1$–0.3) films are also suitable for monolithic devices for electrocaloric cooling, electrostatic energy storage, and pyroelectric energy harvesting (Fig. 8(c)). The relaxor $0.68Pb(Mg_{1/3}Nb_{2/3})O_3$–$0.32PbTiO_3$ (PMN-PT) thin film-based solid-state pyroelectric device that enables the direct measurement of pyroelectric responses and implementation of electro-thermal pyroelectric Ericsson cycles shows the optimized energy density, power density, and Carnot efficiency of 1.06 J/cm^3, 526 W/cm^3, and 19%, respectively [8]. A PyEH made of lead scandium tantalate multilayer capacitors (PST-MLCs) produces 11.2 J of electricity per thermodynamic cycle, which is sufficient to operate the microcontrollers and temperature sensors [23]. Yang et al. [28] experimentally demonstrated the first pyroelectric nanogenerator based on ZnO nanowire (diameters of 200 nm) arrays for harvesting thermoelectric energy with current and voltage coefficients for the ZnO nanowires are $\sim 1.2 - 1.5$ nC/cm^2K and $\sim 2.5 - 4.0 \times 10^4$ V/mK, respectively. The energy conversion characteristic coefficient of the nanogenerator is $\sim 0.05 - 0.08$ Vm^2/W.

Flexible PyEH devices are of interest because of their application in wearable and implantable devices in the human body. Specifically, polymers (e.g., PVDF-TrFE) have been investigated and successfully demonstrated for such applications [38,77–79]. PVDF-based ferroelectric polymers possess both piezoelectric and pyroelectric properties, which make them an excellent choice for flexible hybrid energy harvesters, along with other important properties such as low cost, lightweight, flexibility, biocompatibility, improved mechanical properties, and high sensitivity to small mechanical stimuli. Composites have also been widely investigated, in addition to monolithic polymer pyroelectrics. Chen et al. [77] demonstrated a flexible PMN-PT polymer composite ribbon-based hybrid (piezoelectric and pyroelectric) generator to scavenge the mechanical movements of the human body, as shown in Fig. 9. It consists of micropatterned single-crystal PMN-PT ribbons. The flexible PMN-PT polymer composite ribbon-based sensor was conformally attached to the skin, which enabled high sensitivity to human motion. You et al. [38] demonstrated a non-woven nanofiber-membrane-based (comprising PVDF polymer) self-powered flexible hybrid (piezoelectric and pyroelectric) energy harvester, and the output voltage was recorded using mechanical stresses and temperature changes, as shown in Fig. 9(d)–(f). Zhao et al. [78] reported an output voltage of 9.1 V and a current of 95 nA for a PVDF-based flexible PyEH, which can be used for self-powered chemical exothermic process monitoring applications. In addition, Lee et al. [80] introduced an energy-efficient PVDF-based pyroelectric generator for thermal radiation energy harvesting application, which can be powered by a finger approaching the sensor.

The pyroelectric effect can be combined with other energy generation mechanisms, such as piezoelectric and wind power, to increase the output of harvested energy. Hybrid energy harvesters are more efficient because they use two or more waste-energy sources for energy generation. Lee et al. [81] selected a PVDF-TrFE polymer among many piezoelectric materials because of its excellent pyroelectric and pyroelectric properties, as well as high flexibility and human body temperature

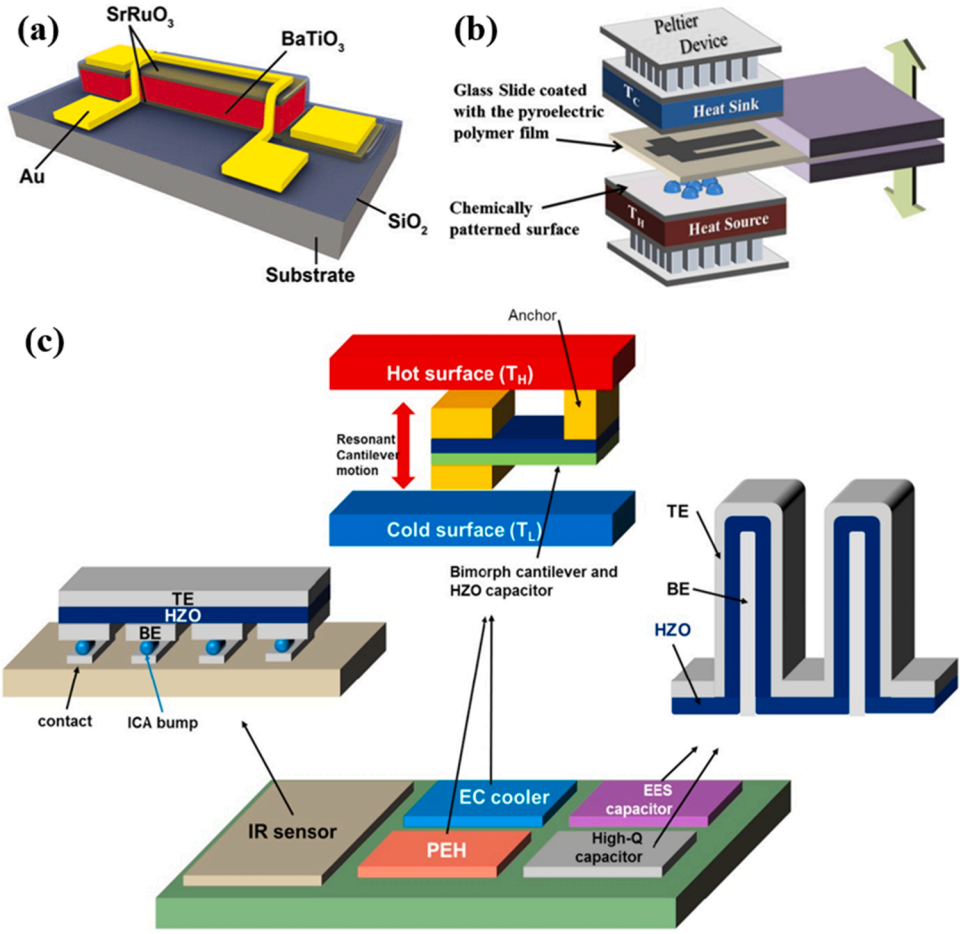

Fig. 8. Schematics of the (a) microfabricated device consisting of a 150 nm thick $BaTiO_3$ film to harvest the energy from the pyroelectric Ericsson thermal-electrical cycles [75] Copyright 2014. *AIP Publishing*, (b) experimental setup for characterizing pyroelectric energy harvesting [71] Copyright 2013. *Elsevier*, and (c) various monolithic devices for pyroelectric energy harvesting and electrocaloric cooling (upper panel), high-charge capacitor and electrostatic energy storage (right panel), and IR sensing (left panel), respectively [76]. Copyright 2015. *Elsevier*.

(thermal energy, pyroelectric) and movements (mechanical energy, piezoelectric), which were used for energy harvesting (Fig. 10 (a) and (b)). You et al. [38] demonstrated a non-woven nanofiber-membrane-based (comprising a PVDF polymer) self-powered flexible hybrid (piezoelectric and pyroelectric) energy harvester. Yang et al. [82] demonstrated flexible hybrid energy harvesters consisting of a solar cell, pyroelectric, and piezoelectric energy harvesters to harvest energy individually or simultaneously from solar, thermal, and mechanical sources. As shown in Fig. 10, (c)–(d), the hydrid cell was fabricated using a PVDF pyro/piezoelelctric film and flexible ZnO nanowire array-poly(3-hexylthiophene) (P3HT) film heterojunction solar cell.

Furthermore, a novel hybrid thermo-magneto-pyroelectric energy generator (TMPyEG) was developed by Choi et al. [83] to harvest waste heat and convert it into electric output via piezoelectricity and pyroelectricity simultaneously, as shown in Fig. 10 (e)–(g). The basic structure of TMPyEG is the same as that of the actuating-type thermomagnetic generator (TMG), which will be reviewed in the next section. Here, the pyroelectric energy conversion material is embedded in the soft magnet to convert the temperature changes directly into electricity.

Pyroelectric solar energy harvesting has also been a prominent research topic over the past few years. A simulation study by Saurabh et al. [84] explored the solar energy harvesting using the lead-free pyroelectric materials. $0.005LaNa_{0.5}Ba_{0.5}TiO_3$-$0.06BaTiO_3$-0.002Ta is found as the best suitable material for energy harvesting. A non-contact, solar-induced pyroelectric nanogenerator (S-PENG) which integrates Au@CNT as solar-thermal layer and polarized PVDF film as pyroelectric layer is developed by Wang et al. [85] which achieves the milliwatt level solar-to-pyroelectric energy harvesting. The high thermal conductivity of CNT accelerates the heat transfer process, while its strong solar-thermal effect can be coupled with the plasmonic effect of Au nanoparticles to obtain a hybrid ensemble with superior light absorption and conversion. This solar-induced pyroelectric nanogenerator successfully generates a notable 1.5 mW/m2 output power under a 200 MΩ load (at 20 °C), thereby overcoming the performance bottleneck of traditional designs with micro-watt power output. Sharma et al. [86] studied several materials with excellent pyroelectric properties for solar energy harvesting. In the study, a square surface plate of the material was placed typically to incident solar radiation. During the heating conditions, convection cooling and solar radiation directly incident on the material's surface is assumed to be natural because of the density difference created by the temperature gradient. The output voltage of the devices was measured when they were subjected to temperature changes (cold and hot air flows), mechanical stresses (compression and bending operations), or both. One of the main challenges for efficient pyroelectric energy harvesting is to provide temporal heat fluctuations to the pyroelectric energy harvesters from a steady heat source. This problem was addressed by Xie et al. [87] designed a wind-driven pyroelectric energy harvester where a propeller was set in rotational motion by an incoming wind stream. Thermal cycling was performed as the reciprocating slider moved the pyroelectric material across the hot and cold zones created by a stationary heat source (lamp) and sink (ambient).

3. Thermomagnetic

3.1. Fundamental principles of thermomagnetic generator

The ferromagnetic materials losing their magnetic properties at a

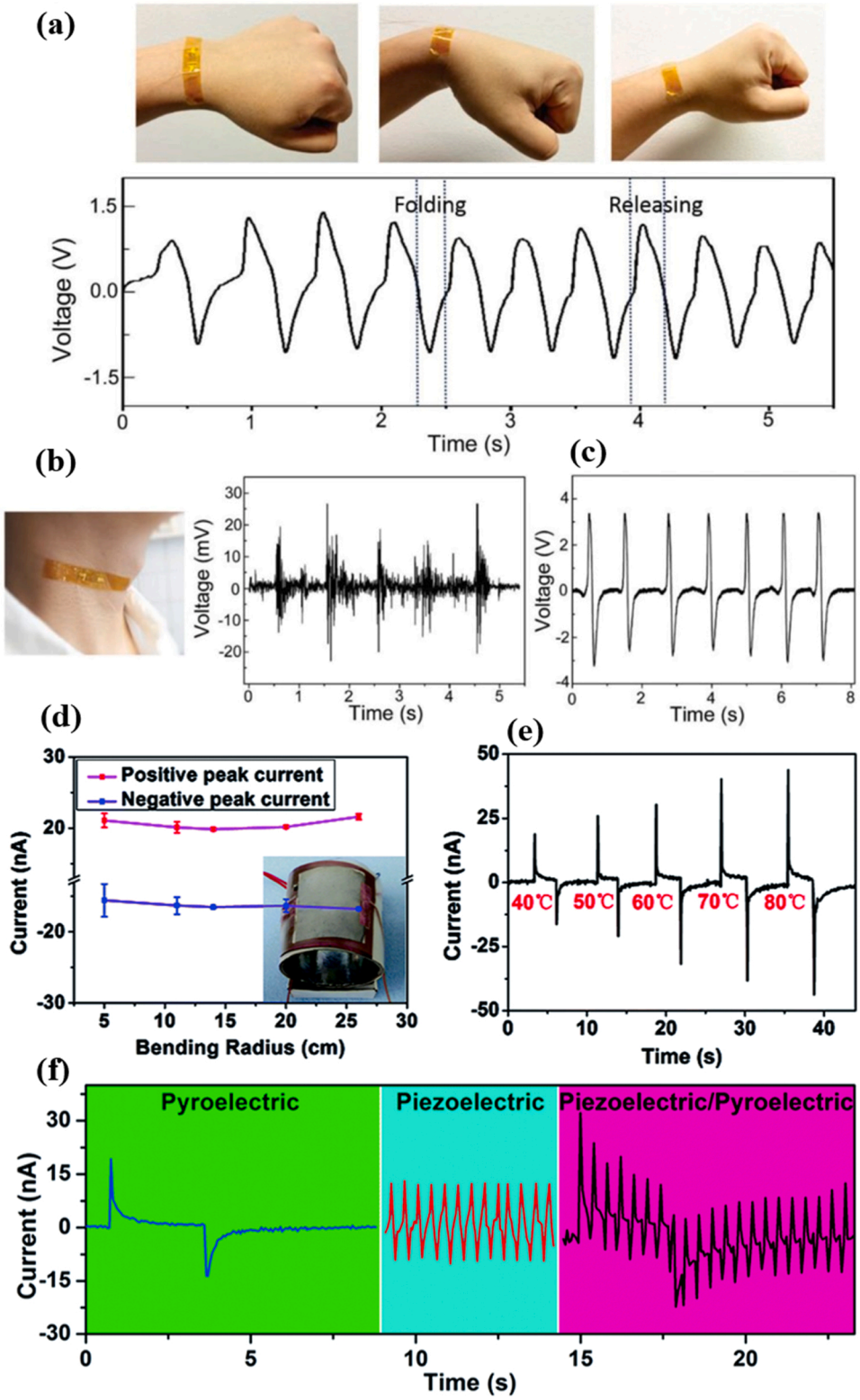

Fig. 9. (a) Images of the PMN-PT ribbon-based pyroelectric flexible device attached to the wrist and the output voltage obtained with wrist actions. Image of (b) device attached to the neck and (c) generated output voltage waveforms from coughing [77]. Copyright 2018. *John Wiley & Sons, Inc.* (d) Output current from the energy harvester with varying bending. (e) Measured output currents of energy harvester when heated from different initial temperatures. (f) Output current from pyroelectric, piezoelectric, and simultaneous effects concerning temperature changes (heating and cooling for 3 s) and mechanical stresses (f = 2.5 Hz) [38]. Copyright 2013. *Royal Society of Chemistry*.

critical temperature are known as the Curie point or the magnetic phase transition point. The Curie temperature (T_c) refers to the temperature at which the spontaneous magnetization in a magnetic material drops to zero and is the critical point at which ferromagnetic or ferrimagnetic materials are transformed into paramagnetic materials. T_c is related to the orderly arrangement of the intrinsic magnetic moments, which can be affected by the intensification of the metal lattice thermal movement depending on the temperature. Different materials have different intrinsic magnetic moment structures, resulting in different T_c.

A thermomagnetic generator (TMG) is designed based on the characteristics of a magnetic material that loses and retrieves its magnetic moment at the Curie temperature (T_c) through temperature fluctuations. Various thermomagnetic generation mechanisms have been proposed based on the rapid magnetic phase transition of magnetic materials at T_c.

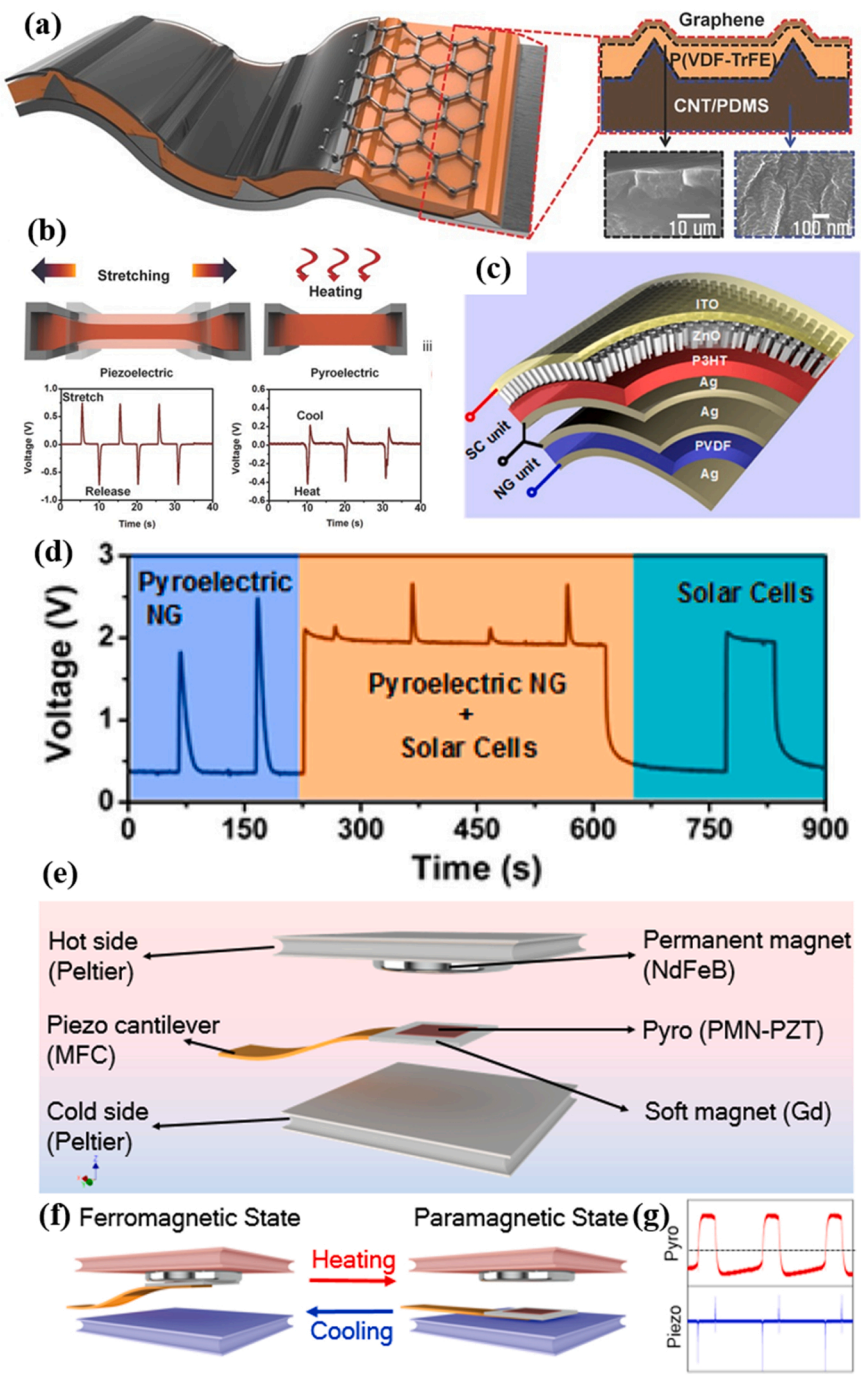

Fig. 10. (a) Schematic illustration of the hybrid stretchable nanogenerators (HSNG). (b) the piezoelectric output voltage from HSNG during stretch-release processes, and the pyroelectric output voltage under a heat stimulus [81]. Copyright 2014. *John Wiley & Sons, Inc.* (c) Schematic diagram of the fabricated hybrid energy cell (piezoelectric, pyroelectric, and solar). (d) The output voltage of the hybrid pyroelectric (after rectification) and solar cells for harvesting thermal and solar energies. . Reprinted (adapted) with permission from [82]. Copyright 2013 American Chemical Society (e) Schematic of TMP^{2}EG showing the heat exchanger part (hot-side Peltier coupled with permanent magnet and cold-side Peltier) and actuating parts (piezoelectric cantilever coupled with soft magnet and pyroelectric material). (f) Schematic of the TMP^{2}EG operation mechanism between the hot and cold sides via thermally induced second-order phase transition of a soft magnet. (g) The pyroelectric continuous output voltage waveform and piezoelectric intermittent output voltage waveform in hybrid TMP^{2}EG [83].

It is no exaggeration to state that the basic concept of TMG began with two great scientists. In the late 18th century, two famous inventors, Thomas Edison and Nikole Tesla also developed and patented numerous designs for TMG [88–91]. Since then, research on TMG has been sparse, but recently, TMG has received significant attention because of the importance of thermal energy harvesting from low-grade heat.

Depending on the operation mechanism, TMG can be divided into two main types: stationary and actuation. The actuation-type TMG includes mechanical moving parts, whereas the stationary TMG does not. Stationary-type TMG (sTMG) energy conversion occurs from thermal to electrical energy. By contrast, in actuation-type TMG (aTMG), energy conversion occurs from thermal to electrical energy with an intermediate mechanical energy step. The sTMG primarily exploits the electromagnetic energy conversion from the rapid magnetic flux change at T_c with a temperature change. On the other hand, the aTMG mainly utilizes piezoelectric energy generation from the mechanical oscillation induced by the magnetic force change of the soft magnetic materials at T_c. Owing to the moving unit, the aTMG has a relatively complex structure compared to the sTMG; however, it is advantageous to maintain a continuous temperature gradient between hot and cold sources.

3.2. *Operation mechanisms of the stationary type and actuation type TMG*

The basic concept of sTMG was first introduced by Nikole Tesla in a patent for pyromagnetic electric generators in 1890 [88]. Fig. 11 (a) shows a schematic diagram of the sTMG in its simplest form, composed of a soft magnetic material and a C-shaped permanent magnet. The

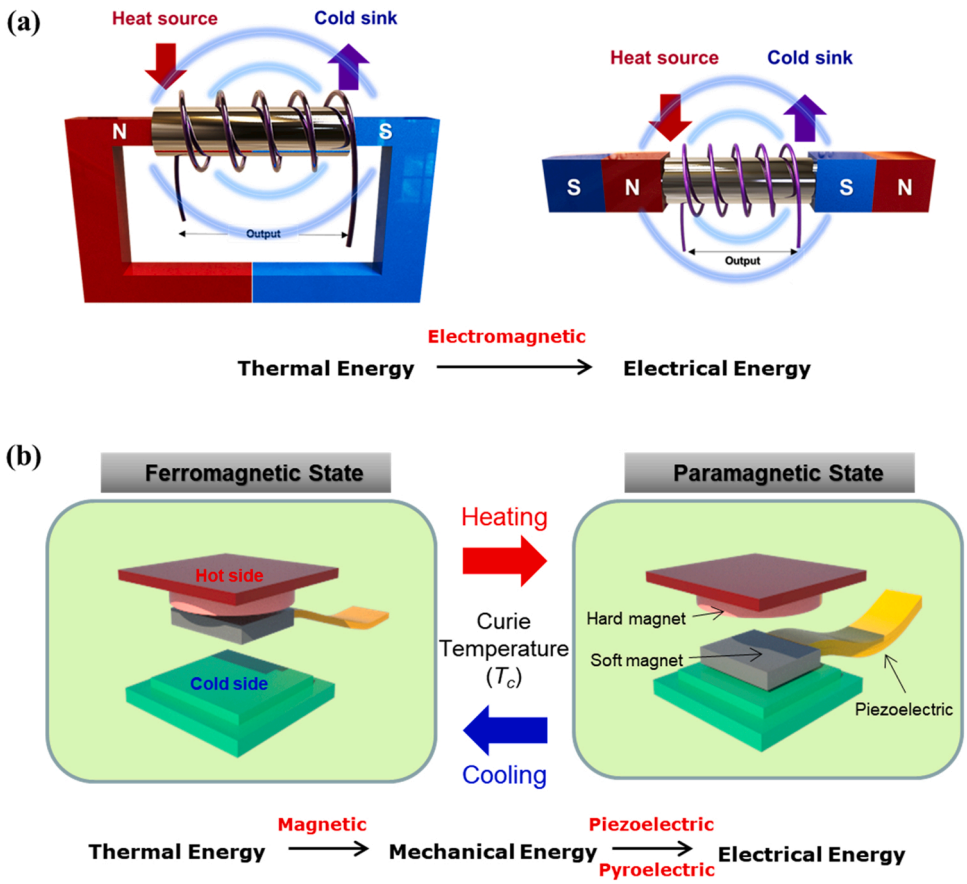

Fig. 11. Operation principles of a thermomagnetic generator (TMG). (a) Schematic diagram of the operation principle of the stationary type TMG. (b) Schematic diagram of the operation principle of the actuation type TMG.

C-shaped permanent magnet can be replaced with two opposing permanent magnets, as shown in the right-side design of Fig. 11 (a). The soft magnetic material is placed between the two poles of the C-shaped permanent magnet or facing the two magnets. The conducting coil, in which the induced current can be generated, is wound around a soft magnetic material. The soft magnetic material can be heated above and cooled below the Curie temperature by contacting to a heat source and a cold sink, respectively. As the temperature increased above T_c, the magnetization of the soft magnetic material approached zero, resulting in the magnetic flux reduction around the coil.

Conversely, when cooled below T_c, the magnetization of the soft magnetic material induced by the permanent magnet increases; thus, the magnetic flux around the coil increases. The magnetic flux around the coil could be switched on and off by alternating the heating and cooling of the soft magnetic material. An alternating induced current can be produced at the two ends of the winding coil through the magnetic materials' cycling temperature. The efficiency of the sTMG is closely related to the magnetic moment of the soft magnetic material, the magnetic flux density of the permanent magnet, and the heat exchange efficiency. For the stable operation of the sTMG, it is essential to consider the structural design in which the soft magnetic material undergoes continuous temperature changes [92].

The basic design of the actuation-type TMG (aTMG), also called the Curie engine or Curie motor was first proposed by Ujihara et al. in 2007 [93]. A schematic representation of a typical aTMG is shown in Fig. 11 (b). The aTMG consists of two main parts: heat exchange and actuating units. The heat-exchange units are composed of a soft magnetic material with a low T_c and a hard permanent magnet with a high T_c. The soft magnetic material is placed between the hot and cold sides. It plays a vital role in producing mechanical oscillation by magnetization and demagnetization, and transferring heat from the hot to cold sides. Gadolinium (Gd) metal is the most commonly used soft magnetic material owing to its low T_c (292.5 ± 0.5 K). The hard magnet is attached to the hot side and provides a magnetic field that attracts soft magnetic material through magnetization. The actuating unit is a spring or cantilever beam connected to the soft magnetic material that pulls downforce to the cold side and includes piezoelectric materials to generate electrical power from the mechanical oscillation. In addition, electrical power generation can be achieved by pyroelectric or triboelectric effects in pyroelectric or triboelectric materials on a soft magnet rather than by the piezoelectric effect.

The fundamental working mechanism of a typical aTMG is shown in Fig. 11 (b). Initially, a soft magnetic material is attached to the permanent magnet on the hot side because it is in a ferromagnetic state below T_c. When it is heated above T_c, it becomes paramagnetic state and loses the attraction force with the permanent magnet. Subsequently, the soft magnetic material was detached and pulled down to the cold side by springs or cantilever beams. In this state, when the soft magnetic material is cooled below T_c on the chilly side, it becomes ferromagnetic state and gains attraction again from the permanent magnet through magnetization.

Consequently, a soft magnetic material is attached to the magnet on the hot side. This continuous heat-exchange cycle is repeated as long as the heat source remains above a specific threshold temperature of T_c of the soft magnet. The oscillation frequency can be determined by the magnetic moment of the soft magnetic materials, the soft magnetic material's heat exchange efficiency, the cantilever's spring force, distance, and temperature gradient between the hot and cold sides. From this periodic mechanical oscillation of soft magnetic materials, electrical energy can be generated through piezoelectric or pyroelectric effects.

Throughout the entire process, thermal energy can be converted into mechanical energy through the thermomagnetic effect. Subsequently, mechanical energy can be converted into electrical energy via mechanoelectrical effects, such as the piezoelectric effect. Similar to thermoelectric generators, aTMG can generate energy from temperature gradients and, unlike thermoelectric generators, are advantageous in maintaining a high-temperature gradient owing to the air gap between the hot and cold sides. Additionally, because the soft magnetic material performs heat exchange from the hot to cold sides along with power generation, aTMG can act as a heat dissipation unit.

3.3. Soft magnetic materials for TMG

The selection of a suitable thermomagnetic material that has the greatest impact on the performance of the TMG is a crucial requirement. For the proper operation of TMG, thermomagnetic materials should generally have several following specific thermal and magnetic properties.

- Soft magnetic materials with low remnant magnetization (M_r).
- Low and adjustable Curie temperature for low-grade heat.
- Significant and rapid magnetization change at Curie temperature.
- High thermal conductivity.
- Low-cost

During the operation cycle, the thermomagnetic materials should be easily demagnetized and magnetized by an external magnetic field. Thus, as shown in Fig. 12 (a), soft magnetic materials without magnetic hysteresis are more advantageous than hard materials with residual magnetization. Additionally, magnetic materials with rapid and large magnetization changes at the Curie temperature have better efficiency. A rapid magnetization change is essential to operate at high efficiency even with a small temperature change, as shown in Fig. 12 (b). In addition, the more significant the magnetization change at T_c, the larger

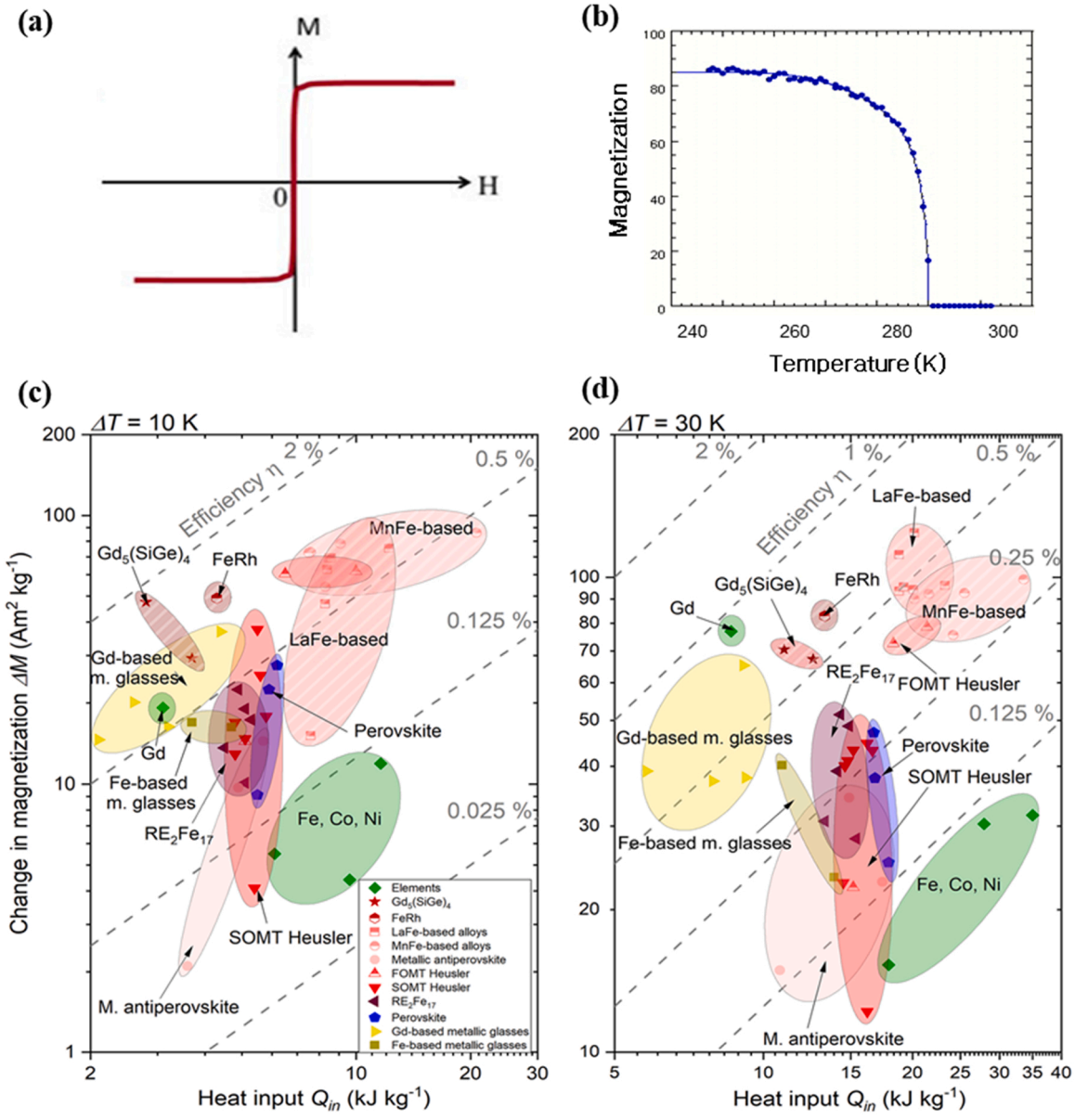

Fig. 12. Thermomagnetic materials. (a) Soft magnetic properties of thermomagnetic materials for TMG. (b) Rapid and large magnetization change at Curie temperature is required. (c) Thermodynamic efficiency (η) of thermomagnetic materials at (c) ΔT = 10 K, and (d) ΔT = 30 K [94]. The $\mu_0 H$ value is fixed at 1 T. Only thermomagnetic materials with phase transition temperatures between 273 K and 373 K were selected. Metallic materials are displayed in shades of red, ceramics in blue, metallic glasses in shades of yellow, and elements in green. Copyright 2021, *AIP Publishing*.

the magnetic flux change; thus, a higher efficiency can be obtained. To apply TMG to low-grade heat, it is necessary to have a low T_c, and the T_c may need to be adjusted according to the application environment. Because the operating temperature must be between T_c and a lower temperature, a thermomagnetic material with T_c near room temperature has better efficiency. Since the TMG operation involves a heat exchange process, the thermal conductivity of the thermomagnetic material is also an important property. Therefore, metal-based thermomagnetic materials are mainly employed in TMG. The price of the thermomagnetic material should also be considered from the perspective of practical applications because rare earth-based magnetic materials are widely used for TMG.

The thermodynamic efficiency of TMG can be defined as the ratio of the available output energy to the heat input energy (Q_{in}) for each cycle.

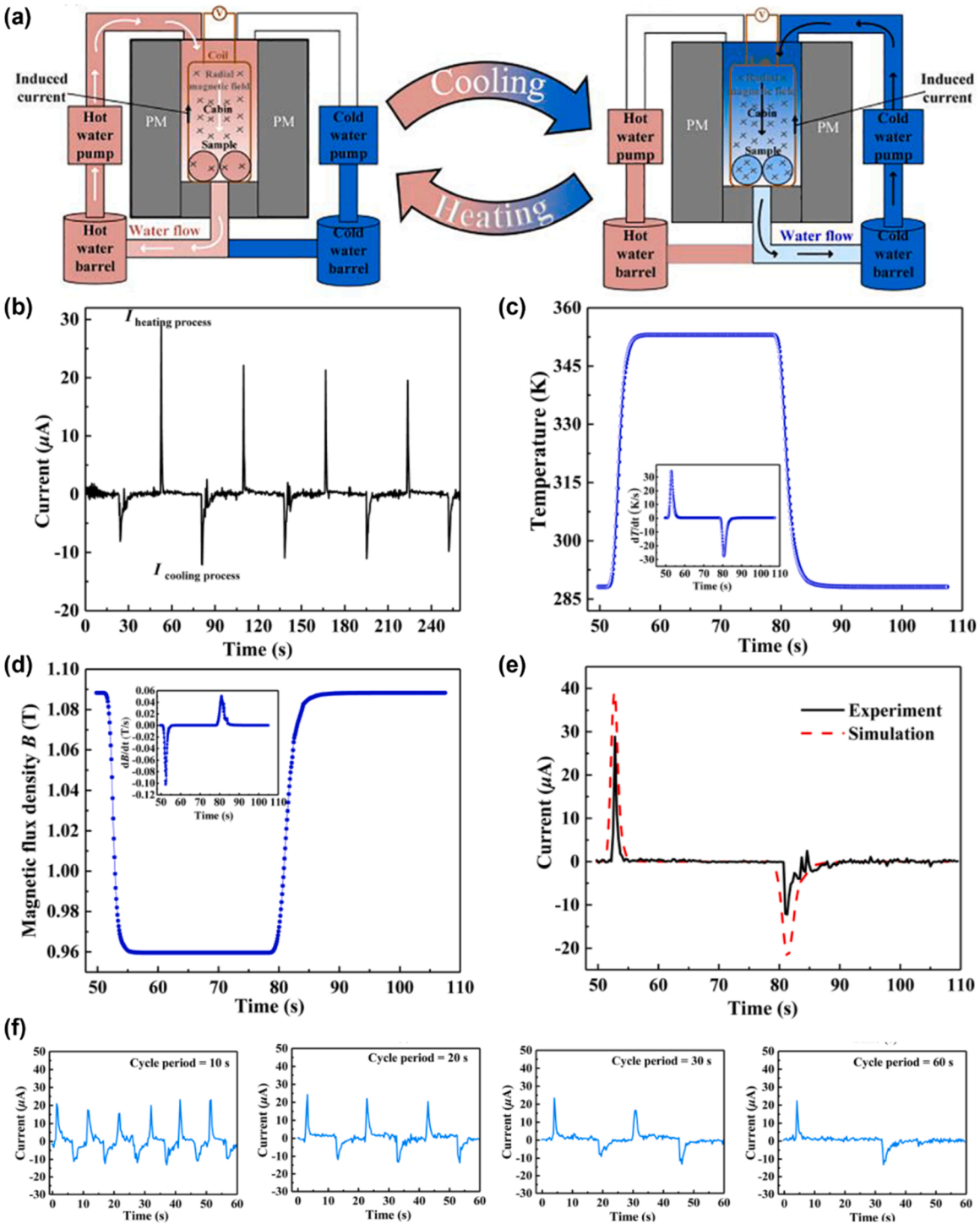

Fig. 13. The active thermomagnetic generator (TMG) with an induction coil. (a) Working principle of the TMG during the heating and cooling processes. (b) The induced current generated by the TMG during the heating and cooling cycles. (c) Simulated sample temperature as a function of time. The inset shows the corresponding dT/dt-t curve derived from the T-t curves. (d) Time dependence of simulated magnetic flux density B during one cycle. The inset shows the corresponding dB/dt-t curve derived from the B-t curves. (e) Comparison of experimental and simulated I-t curves during one heating and cooling cycle. (f) Experimental I–t curves under different cycles of 10, 20, 30, and 60 s, respectively. Reprinted with permission from [96], Copyright 2023, *Elsevier*.

The magnetic energy (E_M) is the upper limit of the output energy in the TMG. Thus, the thermomagnetic material efficiency (η) can be expressed as

$$\eta = \frac{E_M}{Q_{in}} = \frac{\mu_0 \int H dM}{Q_{in}} = \frac{\mu_0 \Delta M H}{\rho \int_{T_C}^{T_H} C_p dT} \quad (8)$$

where μ_0 is the magnetic field constant, ΔM is the change in magnetization, H is the applied magnetic field, ρ is density, and C_P is specific heat capacity [94,95]. Fig. 12 (c) and (d) are Ashby-type plots for efficiency (η) of several thermomagnetic materials as the magnetization change (ΔM) concerning heat input (Q_{in}). The applied magnetic field (H) is not a material property but is related to the MTG device. Thus, in this plot, the $\mu_0 H$ value is fixed at 1 T, which can be easily obtained using common Nd-based permanent magnets. Only thermomagnetic materials with phase transition temperatures (T_c) between 273 and 373 K were selected for application in low-grade thermal energy. It was evaluated for two different temperature gradient values (ΔT) of 10 and 30 K (Fig. 12 (c)). As shown in Fig. 12 (c) and (d), the most efficient materials were located in the top left corner, where η approached 2%. At $\Delta T = 10$ K, materials with a first-order transition (half-solid symbols) reached the highest efficiencies. This is because materials with first-order transitions exhibit sharp magnetic transitions at narrow ΔT values. At $\Delta T = 30$ K, materials exhibiting a second-order transition (solid symbols) tended to show high efficiency. In the case of a low heat input, Gd-based thermomagnetic materials tend to have the highest efficiency at both temperature change values of 10 and 30 K. Notably, the $Gd_5(SiGe)_4$ alloy, the magnetocaloric material, showed the highest efficiency at a low ΔT, as shown in Fig. 12 (c). However, magnetocaloric materials generally have a high heat capacity, which is undesirable for TMG. Therefore, a new paradigm of thermomagnetic materials with low heat capacity and high thermomagnetic efficiency is necessary for high-performance TMG.

3.4. Thermal-energy-harvesting devices with thermomagnetic effect

Stationary-type TMG (sTMG) typically employs an electromagnetic effect using an induction coil surrounding thermomagnetic materials. In an induction coil, an induction current flows to reduce the change in the magnetic flux passing through the coil. Therefore, if a coil is wound around a permanent magnet and a temperature change is induced, energy harvesting is possible by changing the magnetic flux. X. Liu et al. [96] used Gadolinium (Gd)-based hollow cylindrical Halbach permanent magnets. The power performance of aTMG is largely affected by the optimization. Specifically, they reported that energy harvesting performance can be improved more than one order (from 0.16 to 3.6 mW/m^{3}K) by adjusting size and temperature ranges. Fig. 13 (a) shows the mechanism of harvesting thermal energy according to the temperature change by injecting water at different temperatures into cylindrical permanent magnets. At 292 K, the difference in magnetization (dM/dT) was the greatest, so the thermomagnetic generator was operated in the range of 288–353 K. Fig. 13 (b) shows the current change according to the temperature change, Fig. 13 (c) and (d) show the magnitude change of the magnetic flux of the permanent magnet when the temperature is raised and lowered, respectively. Fig. 13 (e) shows the data comparing the current change by the actual experiment and the simulation, indicating that the magnetization change according to the temperature generates the induced existing well. The faster the temperature changes, the faster the magnetic flux changes; thus, more energy can be harvested. As shown in Fig. 13 (f), the magnetization of the permanent magnet changes significantly with the temperature change of the water, and the current is also well harvested. Waske et al. [97] harvested thermal energy using the change in magnetization according to the temperature of the water flowing around the permanent magnet. The composition of La-Fe-Co-Si was fabricated as a thermomagnetic material, and it was used in the construction of an energy harvester together with a permanent magnet of composition Nd-Fe-B. They claimed that a method using 1 permanent magnet and 1 thermomagnetic plate is genus = 1. Likewise, a method using 1 permanent magnet and 2 thermomagnetic plates is genus = 2, and a method using 2 permanent magnets and 2 thermomagnetic plates is genus = 3. In their study, the harvester was produced using the method of genus = 3. In addition, a temperature change of ~30 K was used in the temperature range of 300 K, which is similar to room temperature. In the case of genus = 3, it operated at ~1 Hz, and it was possible to generate a maximum of 1.24 mW of power. Additionally, La(Fe, Si)$_{13}$H$_y$/In, La(Fe, Si)$_{13}$-based compounds with NaZn$_{13}$-type (1:13) structure, are reported to have superior output electrical power density (0.42 mW/m^3) and cost performance (0.102 nW/USD) comparted to those of Gd (0.10 mW/m^3 and 0.005 nW/USD) [98,99]. Furthermore, Joseph et al. [100] reported that scaling of film thickness and device footprint oppositely affect power output. They claimed that electrical power per footprint was increased by 3.4 times by increasing film thickness from 5 to 40 μm of Ni-Mn-Ga, a Heusler alloy film, reaching values of 50 μW/cm2 at a temperature change (ΔT) of only 3 K.

The actuation-type TMG (EMG) heats a permanent magnet to induce mechanical movement. Kishore et al. [101] heated one end of a ring-type magnetic material to change it from a ferromagnet to a paramagnet. Another permanent magnet near the heat source continuously pulled the ring-type magnetic material to generate rotational motion. The power was obtained by operating an axial-flux electric generator by connecting a shaft to the center of a rotating ring-type magnetic material. A magnetic material placed in an ambient-temperature environment of 295 K was heated with 313 K water, and an output of 1.3 mW was obtained at a maximum rotational speed of 14.3 Hz.

Another method of aTMG is to use the thermally induced mechanical oscillation of soft magnetic materials, known as thermo-magneto-electric generators. Suppose a permanent magnet based on a hard magnet with a very high Curie temperature is installed on the hot side, and a soft magnet is placed between the hot and cold sides. In that case, the soft magnet periodically changes to a ferromagnet and paramagnet, causing mechanical vibration. Thermal energy can be harvested using well-known piezoelectric or triboelectric methods. Chun et al. [102] fabricated a harvester by connecting a cantilever to a soft magnet, fixing it to the outside, and attaching PVDF to one side of the cantilever. Fig. 14 (a) shows a harvester composed of a neodymium-based hard magnet and a gadolinium-based soft magnet and its driving principle. Fig. 14 (b) and (c) are photographs of a harvester composed of a bimorph cantilever and array, respectively. The highest voltage was observed when the harvester, composed of arrays, was connected in series (Fig. 14 (d)) and operated at ~3 Hz (Fig. 14 (e)). The maximum power production measured by impedance matching was ~0.158 μW (Fig. 14 (f) and (g)). Song et al. [103] constructed a magneto-thermoelectric generator using $La_{0.85}Sr_{0.15}MnO_3$ and $(Ni_{0.6}Cu_{0.2}Zn_{0.2})Fe_2O_4$ and showed a driving frequency of 0.2 Hz and an output power of 17 μW at a temperature difference of 80 °C. Ujihara et al. [93] and Chun et al. [104] fabricated harvesters with the same structure using gadolinium and neodymium-based magnets. Both studies had a temperature difference of 50 K between the hot side and the cold side and operated at driving frequencies of 28 Hz and 9 Hz and harvested powers of 1.3 nW and 80 μW, respectively.

Triboelectric generators are also useful for harvesting mechanical energy. Through the thermomagnetic method, thermal energy can be converted into rotational or vibrational mechanical energy, and electrical energy can be harvested using triboelectric generators. As shown in Fig. 15, Ahmed et al. [105] harvested thermal energy using a thermomagnetic engine and rotary triboelectric generator. Fig. 15 (a) shows a hybrid energy harvester consisting of a triboelectric generator and an electromagnetic generator with a thermomagnetic engine. As shown in Fig. 15 (b), a triboelectric harvester was fabricated using internal acrylic and external aluminum interdigital electrodes. An alternating current was generated depending on where the internal acrylic plate was located

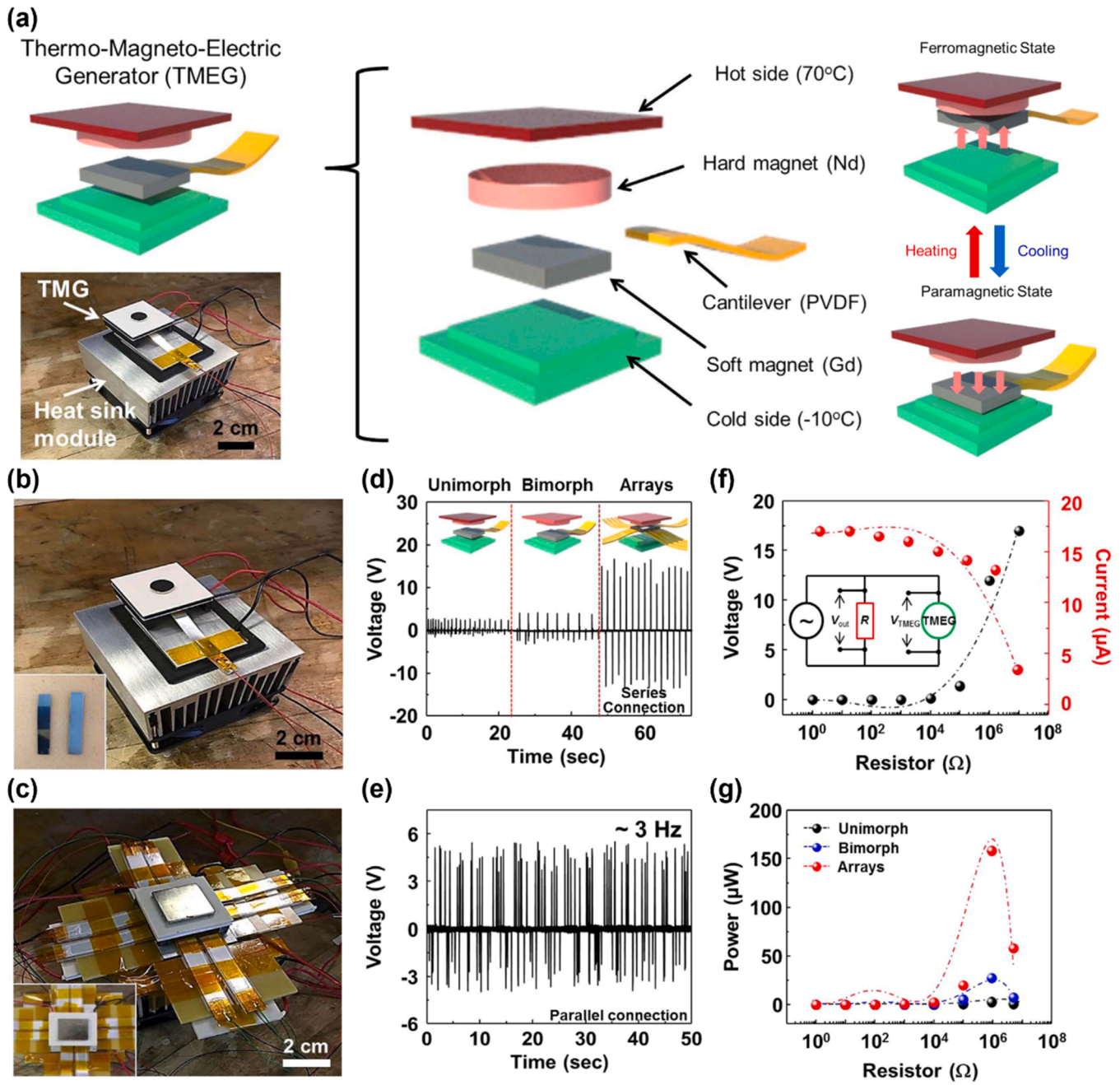

Fig. 14. The thermomagneto-electric generator arrays. (a) Schematic diagram of TMEG. The picture shows a fabricated device image with a heat sink module and schematic representation for TMEG operating through second-order phase transition occurring in soft magnets during periodic cooling and heating. (b) Optical images of fabricated bimorph cantilever-based TMEG and (c) TMEG arrays composed of bimorph cantilevers. (d) Output voltages of unimorph and bimorph cantilever-based TMEG and arrays in series connection. (e) Output voltage and vibration frequency of TMEG arrays in parallel connection. (f) The output voltage and current, and (g) the output power of the unimorph and bimorph cantilever-based TMEG, and arrays with the resistance of external loads from 1 Ω to 10 MΩ. Reprinted with permission from [102], Copyright 2017, *Nature Publishing Group*.

among the two interdigital electrodes. The maximum rotational speed of the shaft according to the hot water temperature was up to 263 rpm (Fig. 15 (c)), and the open-circuit voltage and short-circuit current according to the rpm were 15.6 V and 9.82 μA, respectively (Fig. 15 (d)). The maximum power was 14.4 μW (Fig. 15 (e)). Rodrigues et al. [106] also converted thermal energy into mechanical energy using a hard magnet (NdFeB) and thermomagnet (Gd). An arc-shaped triboelectric generator composed of Nylon 6,6 and Polytetrafluoroethylene (PTFE) was attached to the bottom of the thermomagnet to harvest energy using the triboelectric method. The temperature difference between the hot and cold sides was ~50 °C, and the operating frequency was ~11 mHz. In addition, the generated power was calculated as peak-to-peak power of 358 mW. Cao et al. [107] harvested thermal energy using a ring-shaped structure made of nickel and stainless steel. When one side of the ring is heated to approximately 373 K, and the ring is rotated, the rotor rotates, and the triboelectric harvester composed of fur and fluorinated ethylene propylene (FEP) is operated. The maximum rotational speed was 60 rpm and an output of up to 4.45 mW.

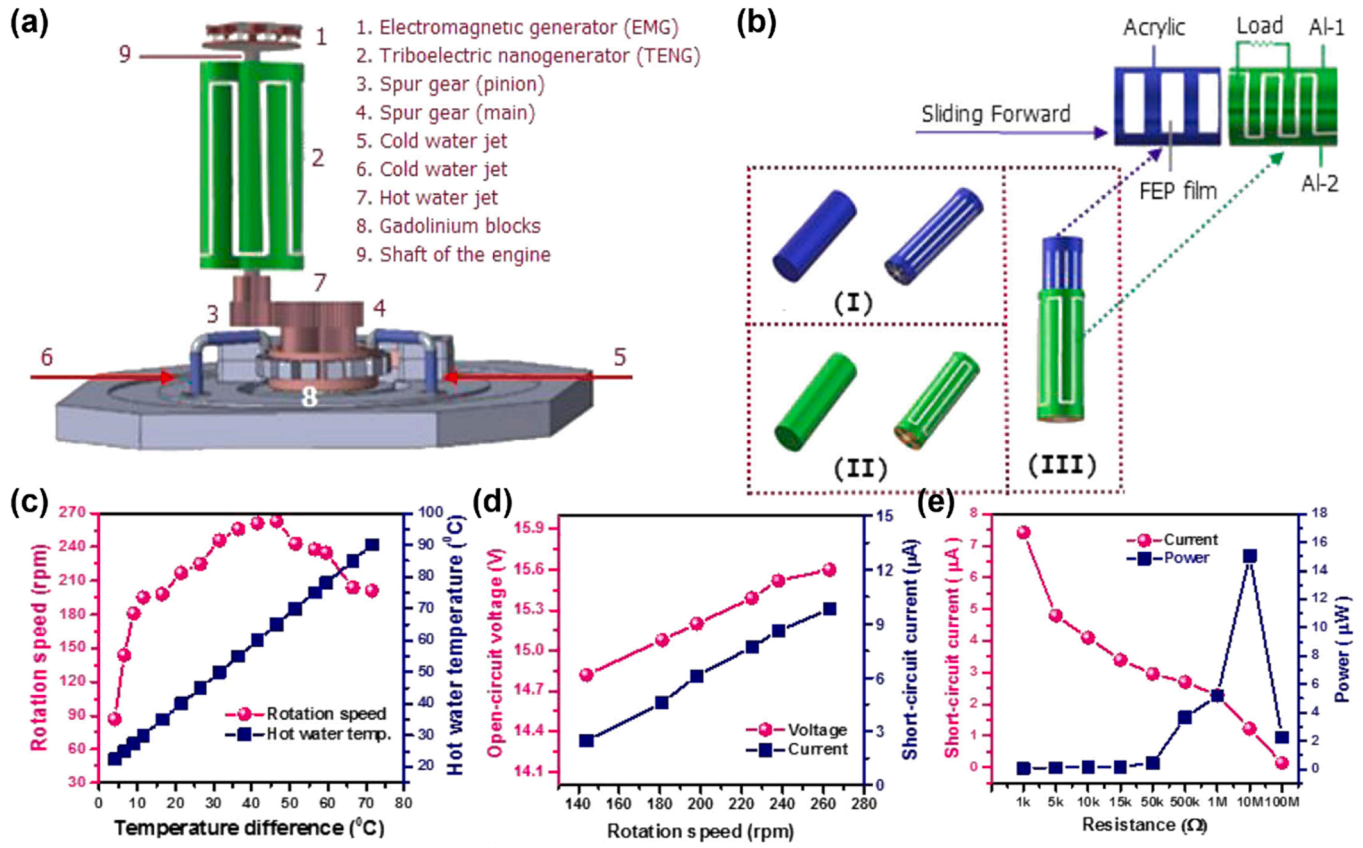

Fig. 15. The thermomagnetic engine with triboelectric nanogenerator. (a) Schematic of the thermomagnetic generator. (b) Schematic diagram illustrating the fabrication process of the triboelectric generator. (c) Temperature difference vs rotation speed. (d) Open-circuit voltage and short-circuit current of the TENG on different rotation speeds. (e) The power output of the TENG at different loads. Reprinted with permission from [105], Copyright 2019, *John Wiley & Sons, Inc.*

4. Thermogalvanic

4.1. Basics of electrochemically driven thermal to electrical energy conversion

Thermogalvanic Energy Harvesters (TGHs) utilize electrode potentials developed between two electrodes under a temperature gradient [108]. The device consists of two identical or distinct electrodes with an electrolyte layer between them. When a temperature gradient is applied, the entropy difference between the two electrodes results in electrochemical potential. The potential differences drive redox reactions, leading to electric voltages and currents being harvested via an externally connected circuit. The figure of merit (*ZT*) derived from thermoelectric devices applies identically to thermogalvanic devices, with thermopower (α) denoting the entropy change associated with ion insertion or redox changes instead of electron addition in the Seebeck coefficients [109]. The device provides unique opportunities due to its inherently low thermal conductivities across the electrolyte layer, yet also exhibits limited ionic conductivities compared to electron migration across thermoelectrics. In addition, the thermopower largely depends on the electrodes (if solids), whereas the thermal conductivities likely depend heavily on the liquid electrolyte phase. This provides a pathway for decoupling the two variables included in the figure of merit.

Several device concepts have been proposed for the TGHs. Similar to the conventional thermogalvanic cells described above, thermally regenerative electrochemical cycles employ a temporal temperature gradient instead of a spatial temperature gradient [110]. The device repeats electrical charging at one temperature and discharges at another, completing the thermodynamic cycle. Such thermodynamic cycles, similar in principle to Rankine cycles, require electrical charging and discharging systems to be implemented in the device. Another variant involves thermogalvanic pseudocapacitors, which utilize the adsorption and desorption of ionic species at different temperatures [111]. In this type, the electrode surface and electrolyte conditions dominate the adsorption behavior, governing the thermopower. This section reviews a few research efforts to improve the thermopower and various novel device designs, focusing on demonstrations of real-life applications.

4.2. Materials development for thermogalvanics in terms of thermopower

Linford et al. [112] studied various Li-ion battery electrode materials in terms of their thermopower and showed that many Li-containing solids exhibit similar thermopower between 1.2 mV/K and 2.1 mV/K. The studied materials include metallic solids such as pure Li [113] or Li-Al [114] alloys and ceramics such as $LiCoO_2$ [115], $Li_xV_2O_5$ [116], $LiFePO_4$ or $Li(Ni_xMn_yCo_z)O_2$ electrodes. The thermopower of these materials is interpreted in terms of the partial derivative of the lithium chemical potential with respect to temperature, namely the partial molar entropy of lithium. A similar thermopower across a wide range of solid-state chemistries shows that engineering the partial molar entropies of solids is inherently difficult. On the other hand, liquid electrolytes exhibit a large thermopower on average. Bonetti et al. showed that the thermopower of nonaqueous electrolytes consisting of 0.1 M tetrabutylammonium nitrate in 1-dodecanol reaches up to 7 mV/K, supporting the entropic interpretation of thermopower [117].

Another heavily researched electrode choice for thermogalvanics is solvated ferri/ferrocyanides ($[Fe[CN]_6]^{3-}/[Fe[CN]_6]^{4-}$)[118]. When solvated in water, the redox couple underwent potential changes of ~1.4 mV/K. Duan et al. [119] showed that thermopower could be engineered significantly by incorporating various molecules into ferricyanide solutions (Fig. 16). Adding guanidinium to 0.4 M [Fe

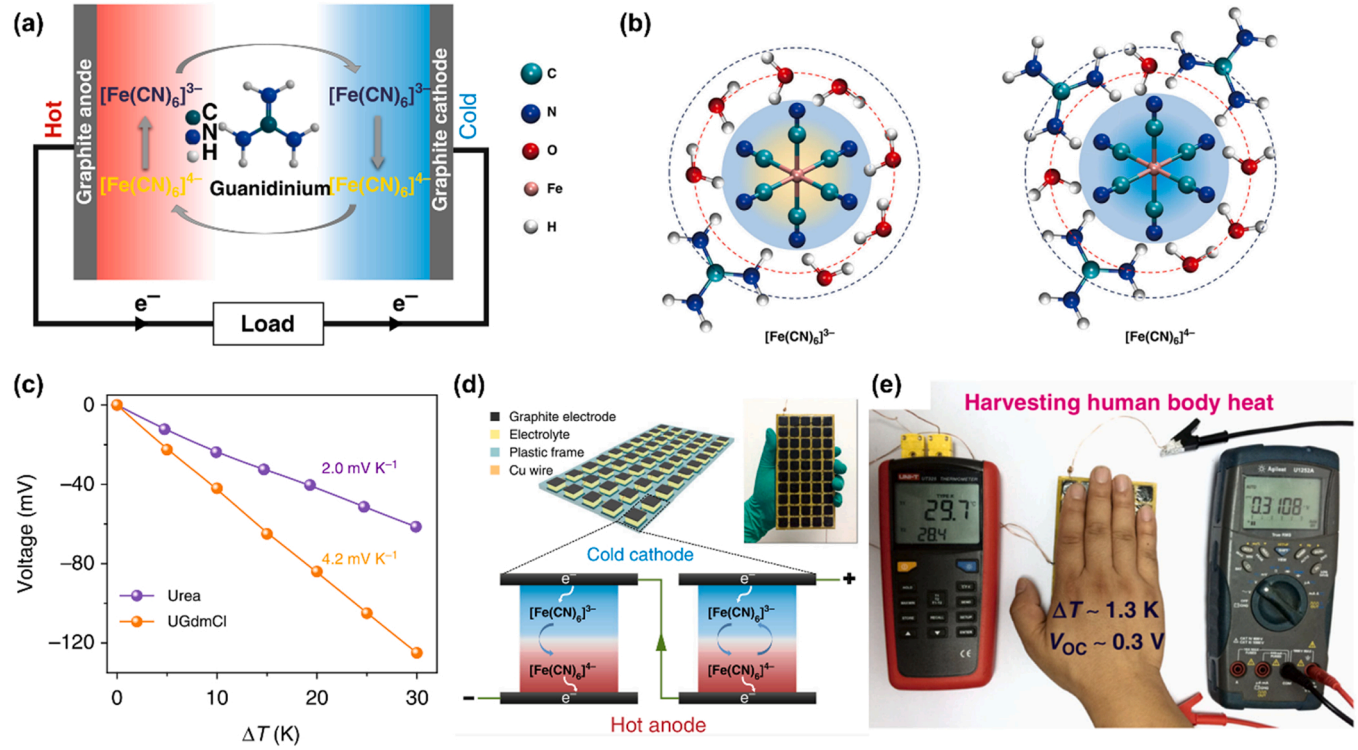

Fig. 16. (a) Schematic illustration of guanidinium-engineered ferri/ferrocyanides and the TGH utilizing the molecules (b) Molecular view of the engineered redox couples and their entropy increase mechanisms (c) the increased thermopower upon addition of guanidinium and urea to the redox couple (d) array design of the TGHs and (e) the device generating 0.3 V by human hand touching [119]. Reproduced with permission [119]. Copyright 2018. Nature Publishing Group.

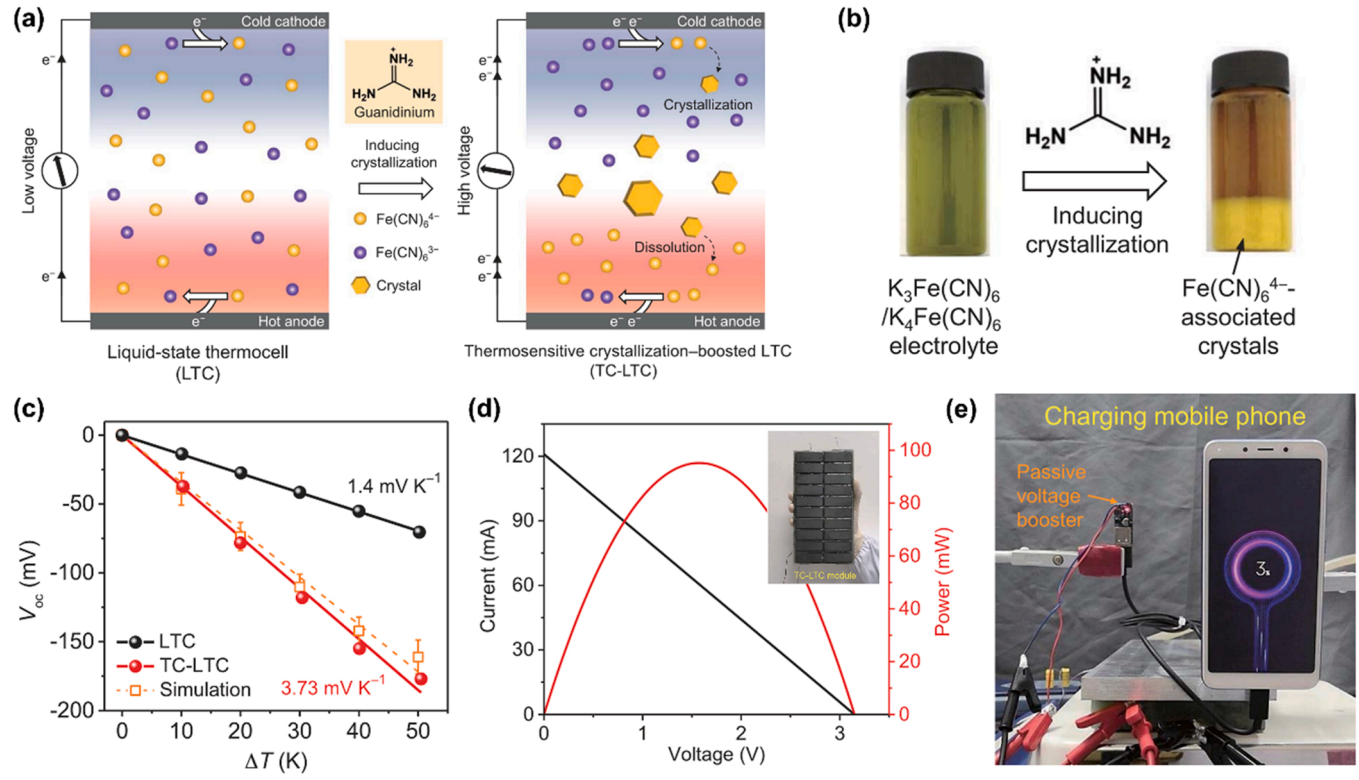

Fig. 17. (a) Schematic illustration of thermosensitive crystallization-boosted liquid thermocells (b) Pictures showing the guanidinium cation-induced crystallization and phase separation (c) the increased thermopower upon addition of thermal crystallization (d) the output power characteristics of TGH arrays (e) the device demonstrating cell phone charging under 50 K temperature gradient [120]. Reproduced with permission [120]. Copyright 2020. AAAS.

$[CN]_6]^{3-}$/$[Fe[CN]_6]^{4-}$ solutions resulted in a thermopower of 2.7 mV/K. Incorporating urea molecules into guanidinium-added ferricyanide solutions further increases the thermopower to 4.2 mV/K. The authors developed a prototype module with 50 unit devices connected in series based on these materials. The module design is essentially similar to that of thermoelectric modules, with a hot-sided anode and cold-sided cathode plates. Simply placing hands on the module results in a temperature gradient of 1.3 K and the generated open circuit voltage of 0.3 V from the module. Aqueous devices are considered promising as a safe and low-cost means of low-grade heat.

Another means of optimizing ferri/ferrocyanides was reported by Yu et al. [120], based on the fact that ferrocyanides ($[Fe[CN]_6]^{4-}$) selectively crystallize with the addition of guanidinium cations on the cold side (Fig. 17). The device places the cold-side cathode on top, which induces crystallization. The crystallites then fall to the bottom hot-side anode owing to gravity and dissolve back into the electrolyte due to increased solubility. The overall cycle results in enhanced thermopower of 3.7 mV/K as opposed toinstead of pristine 1.4 mV/K for 50 K temperature differences. The device generated up to 11.1% of the Carnot efficiency. The twenty-cell-incorporated module generates a short-circuit current of 120 mA and an open-circuit voltage of > 3 V, demonstrating cell phone charging and a thermohydrometer. Notably, the crystallization-induced thermogalvanic device provides a strategy to enhance the thermopower while reducing the thermal conductivity and maintaining the ionic conductivity, demonstrating potential strategies toward decoupled physical properties comprising the figure of merit.

Several other studies have optimized the liquid properties to enhance thermopower. Han et al. [121] demonstrated polarized electrolytes based on KCl, methylcellulose (MC), and I^-/I_3 redox couples that exhibit the n-type thermopower of 8.18 mV/K and p-type thermopower of 9.62 mV/K. Salt-induced molecular complex formation leads to notable entropy changes in temperature and, thus, high thermopower. The device generated an open circuit potential of 134 mV and 80.5 μA between 24 and 43 °C. Another study demonstrated mixed thermogalvanic and thermodiffusion (Soret) effects in ionic gelatin [122]. The measured thermopower of the gelatin-ferricyanide mixture reaches 4.8 mV/K, and that of gelatin-KCl is 6.7 mV/K. (Note that the gelatin/KCl mixture has no redox-active elements; thus, the thermopower generated is attributed to thermodiffusion.) When gelatin was mixed with KCl and ferri/ferrocyanides, the maximum thermopower of 17.0 mV/K was achieved. This work demonstrates that several mechanisms (in this case, the thermogalvanic and Soret effects) may be engineered to provide synergistic effects in liquid thermogalvanics.

4.3. Novel device concepts for thermogalvanic devices

In addition to optimizing thermogalvanic materials, several novel device concepts have been proposed. Linford et al. [123] demonstrated that two battery stacks connected in series at two different temperatures could be utilized to harvest the temperature difference (Fig. 18). Initially at an identical potential, the temperature difference between the two batteries creates a potential difference that can be harvested through an external circuit. Once the two batteries reach equilibrium potential, mechanically swapping their positions (and thus the temperatures) re-creates potential differences, which can be harvested again. Repeating these cycles efficiently harvests the temperature gradient into electrical energy using regular (or even recycled) batteries. They demonstrated that similar concepts are also applicable to temporal temperature gradients instead of spatial temperature gradients, with the two batteries placed under identical yet temporally varying temperatures. With two $LiCoO_2$/Li batteries and 100 Ω resistors, they obtained up to 45 μA and 0.4 μW power.

Similarly, Poletayev et al. [124] demonstrated a continuous electrochemical heat engine using flow-type battery devices. Two flow-type batteries made of $V^{2+/3+}$ redox couple and $Fe(CN)_6^{3-/4-}$ redox couple was separated across ion-selective membranes and installed on both the cold and hot sides. The two flow cells undergo charge and discharge redox reactions at high and low temperatures, respectively, while simultaneously allowing the exchange of working fluids across high and low temperatures. This unique design decouples thermal and electrical entropy generation, resulting in a continuously operating electrochemical heat engine. The open circuit potential reached slightly over 100 mV across 10 and 50 °C, and the short circuit current density exceeded 3 mA/cm^2. With engineered fluids to match specific temperatures, the device design can be applied to various temperature regimes. In addition, a device operating in reverse cycles is analogous to electrochemical cooling.

5. Comparisons and future research projections

While it is challenging to compare the effectiveness of the aforementioned thermal energy harvesting approaches under identical conditions, reasonable efficiency analysis can be instrumental in providing comprehensive knowledge in low waste heat energy recovery. It should be noted that the following analysis does not prioritize one method over another, as conversion efficiency depends on the working temperature range, material properties, and thermal cycles. In energy harvesting,

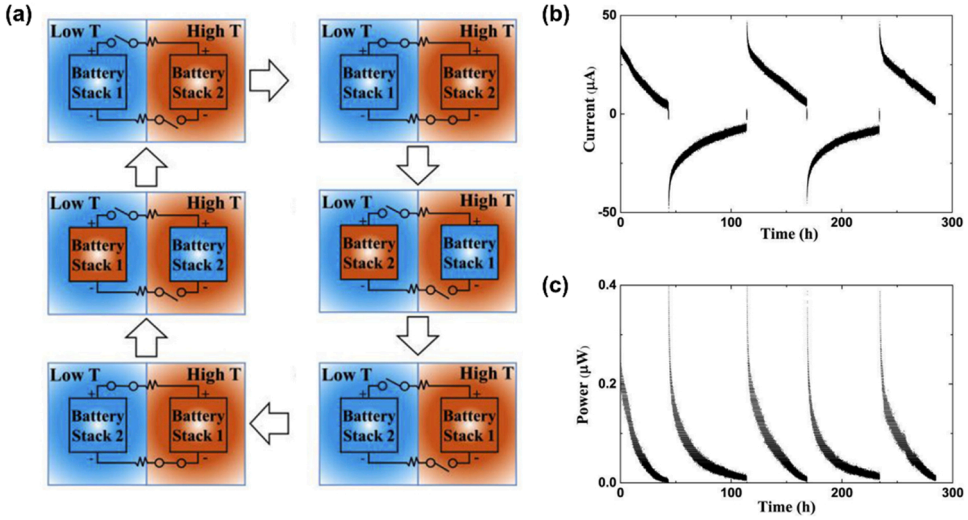

Fig. 18. (a) Schematic illustration of multi-cell thermogalvanic systems operating under dual-temperature mode and their (b) current output and (c) power output generated under a 30 K temperature difference [123]. Reproduced with permission. [123] Copyright 2018. Elsevier.

efficiency pertains to the conversion from thermal to electrical energy. With regard to conversion efficiency, the upper bound of thermal-to-work conversion efficiency is given as Carnot efficiency (η_{carnot}).

In pyroelectric energy harvesting, the efficiency can be directly estimated by the electro-thermal coupling factor (k^2), which varies from 0.1% to 5% in each material at 298 K [126,127]. In practical thermal cycles, the pyroelectric energy harvester's efficiency is claimed to be

$$\eta_{pyroelectric} = \frac{p^2 T_{hot}}{\rho C_P \varepsilon_{33}^{\sigma}} \times \frac{T_H - T_C}{T_H} = k^2 \times \eta_{carnot} \tag{9}$$

where p, ρ, C_P, $\varepsilon_{33}^{\sigma}$, T_H and T_C are pyroelectric coefficient, density, specific heat capacity, dielectric permittivity, hot and cold side temperature, respectively [128].

In practice, for PMN-PT, a widely studied pyroelectric material, if we assume T_H is 298 K and $T_H - T_C$ is 30 K ($\eta_{carnot} \sim 10\%$), we can expect $< 1\%$ of efficiency for pyroelectric energy harvesting in low-waste heat temperature regimes [68].

In the case of thermomagnetic principle, the efficiency can be described as:

$$\eta_{thermomagnetic} = \frac{\mu_0 \int H dM}{\rho \int_{T_C}^{T_H} C_p dT} \tag{10}$$

where μ_0 is the magnetic field constant, ΔM is the change in magnetization, H is the applied magnetic field, ρ is density, and C_P is specific heat capacity [94,95]. Here, the numerator represents work in electromagnetic induction and the denominator represents absorbed heat in a thermomagnetic material during heating. In the case where T_H is 298 K and $T_H - T_C$ is 30 K, efficiency and Carnot-relative efficiency is about 2% and 20%, respectively [94].

Finally, thermogalvanic conversion efficiency can be derived by

$$\eta_{thermogalvanic} = \frac{P_{\max}}{k_{eff} A \left(\frac{T_H - T_C}{d}\right)} \tag{11}$$

where $P_{\max}$, k_{eff}, A and d are thermogalvanic power output, effective thermal conductivity, cross-sectional area and inter-electrode distance of the device [120]. In the study, this analysis, the highest efficiency is reported to be 11% of Carnot efficiency. Table 4 provides a rough comparison of the efficiencies between thermal energy harvesting principles.

The efficiency of all three approaches falls within a range of approximately 10% of the Carnot efficiency. This indicates that there is still a significant gap between current reported performance and the theoretical limit, as defined by the Carnot efficiency. To perceive an innovative thermal energy harvester, perspectives on material science and structural device design must be considered. For example, pyroelectrics can provide a high power density for small devices. The high performance of pyroelectrics can be achieved by (1) a rapid ferroelectric phase transition that enables high efficiency, (2) a low leakage current preventing losses, and (3) a high breakdown voltage [23]. The current challenge is to enhance the performance of pyroelectric energy harvesters and efficiently harvest low-grade waste heat by improving p and FoMs. This can be achieved by reducing the material's dielectric constant by adding suitable dopants and increasing the porosity (low density) using pore-forming methods. Currently, more attention is being paid to fabricating porous pyroelectric materials for future PyEHs. Material (change in composition) and geometrical modification approaches are ongoing to improve pyroelectricity. To generate more power, hybridization with other energy conversion mechanisms and thermal-energy-harvesting devices can be a solution. It is also challenging to provide continuous temperature fluctuations to PyEHs, which can be solved by environmental airflow cooling or using a cantilever-type assembly (mechanical sources). There is still plenty of room for improvement in these methods for high pyroelectric harvesting power. Polymer-based or composite-structured pyroelectric materials can be used for flexible thermal energy harvesting to power wearable sensors and keep track of human health. A new application of the pyroelectric effect has emerged in applications related to electrochemical catalysis. The generated electrical charge and electric potential in pyroelectrics can be used as power sources for electrochemical reactions in bacterial elimination, water and air purification, and hydrogen generation [30].

The performance of a thermomagnetic generator (TMG) is affected mainly by selecting a suitable thermomagnetic material. Materials should have low remnant magnetization (M_r), adjustable Curie temperature for low-grade heat, high thermal conductivity, and low manufacturing costs. Additionally, magnetic materials with rapid and large magnetization changes at the Curie temperature have better efficiency. A rapid magnetization change is essential to operate efficiently, even with a slight temperature change. In addition, the larger the magnetization change at T_c, the more significant the magnetic flux change; thus, a higher efficiency can be obtained. To apply TMG to low-grade heat, it is necessary to have a low Curie temperature, which may need to be adjusted according to the application environment. Because the TMG operation involves a heat exchange process, the thermal conductivity of the thermomagnetic material is also an important property. Therefore, metal-based thermomagnetic materials are mainly employed in TMG. The price of the thermomagnetic material should also be considered from the perspective of practical applications because rare earth-based magnetic materials are widely used for TMG.

Over the past decade, research into thermogalvanic energy harvesters has observed significant improvements in materials with high thermopower, mechanisms entailing one or more individual physical effects, and device concepts, including multi-cell and continuous operation. Potential future research projections include further material development in solid-state thermogalvanic materials and synergistic design of thermally driven electrochemical phenomena. On the materials side, development has been focused on liquid-based electrolytes, including aqueous ferri/ferrocyanides, ionic gelatines, and dissolved multi-cellulose. While liquid-based thermogalvanics have proven to have high thermopower, they present inherently low volumetric and gravimetric power densities compared to solid-based thermogalvanics. This is inherently difficult to overcome for most liquid-based electrodes, and high-density solid electrodes need to be developed. In terms of physical mechanisms, it remains challenging to separate and decouple the thermogalvanic effects, Soret effects, and thermally induced pseudocapacitance in electrochemical systems. The measured voltages due to a temperature gradient are a complex manifestation of all three

Table 4
Comparison of the energy conversion mechanisms efficiency analysis.

Ref.	*Thermal energy harvesting methods*	*Efficiency*	*Estimated efficiency at 298 K (T_H), 30 K (ΔT)*
	Carnot cycle	$\eta_{carnot} = \frac{T_H - T_C}{T_H}$	$\sim 10\%$
[126–128]	*Pyro-electric*	$\eta_{pyroelectric} = \frac{p^2 \quad T_{hot}}{C_V \varepsilon_{33}^{\sigma}} \times \frac{(T_H - T_C)}{T_H} = k^2 \times \eta_{carnot}$	$< 1\%$
[94,95]	*Thermo-magnetic*	$\eta_{thermomagnetic} = \frac{\mu_0 \int H dM}{\rho \int_{T_C}^{T_H} C_p dT} = \frac{\mu_0 \int H dM}{\rho C_P T_H} \frac{1}{\eta_{carnot}}$	$\sim 2\%$
[120]	*Thermo-galvanic*	$\eta_{thermogalvanic} = \frac{P_{\max}}{\frac{k_{th} A}{d}(T_H - T_C)} = \frac{P_{\max}}{\frac{k_{th} A}{d} \frac{(T_H - T_C)^2}{T_H} \eta_{carnot}}$	$\sim 1\%$

mechanisms in action, yet their relative contributions or potential destructive interference remain mostly uncovered. Decoupling and separately engineering the individual mechanisms shall lead to elaborate materials design guidelines for high-power thermogalvanics.

6. Conclusion

Low-grade waste-heat recovery is expected to become a key component of the power conversion and electricity generation industry owing to its massive energy loss. However, conventional heat recovery approaches, such as heat pumps and thermoelectrics, have yet to recapture low-grade waste heat effectively. Instead, other thermal-energy-harvesting mechanisms, such as pyroelectrics, thermomagnetics, and thermogalvanics, can be more suitable options for low-grade waste-heat recovery. Growing attention on solid-state thermal energy harvesting is due to its strength in low-grade waste-heat recovery. Both pyroelectric and thermomagnetic energy harvesting is advantageous in transient temperature condition whereas thermogalvanic can be used for steady temperature gradient condition, similar to thermoelectrics. Accordingly, intermittent low-waste heat disposal areas, such as exhaust from manufacturing factory, are feasible areas where pyroelectric and thermomagnetic mechanisms are promising. On the other hand, a thermogalvanic mechanism can be applicable to the fields where thermoelectrics are implemented, such as spacecraft, heat pipe, heating and air conditionings. These robust solid-state devices are advantageous for miniaturization and maintenance. They can be installed near low-grade waste heat sources, where the power density is low but ubiquitous. In brief, this review covers broad topical areas under pyroelectric, thermomagnetic, and thermogalvanic conditions. For each topic, a detailed analysis is provided, comprising the essential physics, working principles, material development, and device performance. In addition, the guidance of future research projections to increase the figure of merit for materials and thermopower is described.

CRediT authorship contribution statement

S. Hur: Investigation, Data curation, Resources, Visualization, Writing – original draft, Writing – review & editing. **S.Kim:** Investigation, Data curation, Resources, Visualization, Writing – original draft, Writing – review & editing **H.-S.Kim:** Data curation, Resources, Visualization, Writing – original draft. **A.Kumar:** Data curation, Resources, Visualization, Writing – original draft. **C.Kown:** Data curation, Resources, Visualization, Writing – original draft. **J. Shin:** Data curation, Resources, Visualization, Writing – original draft. **H. Kang:** Resources, Writing – review & editing. **S.-T.Hyun:** Resources, Writing – review & editing. **J.Ryu:** Investigation, Data curation, Resources, Visualization, Writing – original draft, Writing – review & editing. **J.-M.Baik:** Project administration, Validation, Supervision, Writing – original draft, Writing – review & editing. **H.-C. Song:** Project administration, Validation, Supervision, Writing – original draft, Writing – review & editing.

Declaration of Competing Interest

The authors declare that they have no known competing financial interests or personal relationships that could have appeared to influence the work reported in this paper.

Data Availability

Data will be made available on request.

Acknowledgements

S.H. and S.K. contributed equally to this work. S.H., H.-S.K., J. S., J. M.B and H.-C.S. would like to acknowledge the support from the National R&D Program through the National Research Foundation of Korea (NRF) funded by the Ministry of Science and ICT (NRF-2021R1C1C1009100, NRF-2020M3H4A3105594) and the Korea Institute of Science and Technology (2E32491, 2E32524, 2E32543, 2V09293). A. K. and J. R. acknowledges the support from the National Research Foundation of Korea (NRF-2023R1A2C2005864). S.K., C. K., and S.T.H. acknowledges support from the Hanyang University (HY-202100000002985).

Appendix A. Supporting information

Supplementary data associated with this article can be found in the online version at doi:10.1016/j.nanoen.2023.108596.

References

[1] UNFCCC, Adoption of the Paris agreement. Proposal by the President, 2015.
[2] C.F. Schleussner, et al., Science and policy characteristics of the Paris Agreement temperature goal, Nat. Clim. Change 6 (9) (2016) 827–835.
[3] IEA, World Energy Outlook, 2022.
[4] IEA, Global Energy Review (2021).
[5] IEA, World Energy Balances, 2022.
[6] The Energy Flow Chart Released by Lawrence Livermore National Laboratory. 2021 [cited 2023; Available from: ⟨https://flowcharts.llnl.gov/commodities/energy⟩.
[7] A. Firth, B. Zhang, A.D. Yang, Quantification of global waste heat and its environmental effects, Appl. Energy 235 (2019) 1314–1334.
[8] S. Pandya, et al., Pyroelectric energy conversion with large energy and power density in relaxor ferroelectric thin films, Nat. Mater. 17 (5) (2018) 432.
[9] Fermi, E., Thermodynamics. 2012: Courier Corporation.
[10] Cresko, J., et al., Innovating clean energy Technologies in advanced manufacturing. Quadrennial Technology, 2015.
[11] Johnson, I., W.T. Choate, and A. Davidson, Waste heat recovery. Technology and opportunities in US industry. 2008, BCS, Inc., Laurel, MD (United States).
[12] Thekdi, A. and S.U. Nimbalkar, Industrial waste heat recovery-potential applications, available technologies and crosscutting r&d opportunities. 2015, Oak Ridge National Lab.(ORNL), Oak Ridge, TN (United States).
[13] D.V. Singh, E. Pedersen, A review of waste heat recovery technologies for maritime applications, Energy Convers. Manag. 111 (2016) 315–328.
[14] Y. Li, et al., A technology review on recovering waste heat from the condensers of large turbine units in China, Renew. Sustain. Energy Rev. 58 (2016) 287–296.
[15] H. Jouhara, et al., Waste heat recovery technologies and applications, Therm. Sci. Eng. Prog. 6 (2018) 268–289.
[16] Y. Ammar, et al., Low grade thermal energy sources and uses from the process industry in the UK, Appl. Energy 89 (1) (2012) 3–20.
[17] M. Papapetrou, et al., Industrial waste heat: estimation of the technically available resource in the EU per industrial sector, temperature level and country, Appl. Therm. Eng. 138 (2018) 207–216.
[18] F. Hao, et al., High efficiency Bi_2Te_3-based materials and devices for thermoelectric power generation between 100 and 300 degrees C, Energy Environ. Sci. 9 (10) (2016) 3120–3127.
[19] Z.L. Bu, et al., A record thermoelectric efficiency in tellurium-free modules for low-grade waste heat recovery, Nat. Commun. 13 (2022) 1.
[20] R.A. Kishore, S. Priya, A review on low-grade thermal energy harvesting: materials, methods and devices, Materials 11 (2018) 8.
[21] Z.Y. Xu, et al., Double-section absorption heat pump for the deep recovery of low-grade waste heat, Energy Convers. Manag. (2020) **220**.
[22] D.M. van de Bor, C.A.I. Ferreira, A.A. Kiss, Low grade waste heat recovery using heat pumps and power cycles, Energy 89 (2015) 864–873.
[23] P. Lheritier, et al., Large harvested energy with non-linear pyroelectric modules, Nature 609 (7928) (2022) 718.
[24] Y. Yang, Pyroelectricity gain in multilayers, Nat. Energy 7 (11) (2022) 1007–1008.
[25] Zheng, Z.H., et al., Harvesting waste heat with flexible Bi2Te3 thermoelectric thin film. Nature Sustainability, 2022.
[26] O.H. Ando, A.L.O. Maran, N.C. Henao, A review of the development and applications of thermoelectric microgenerators for energy harvesting, Renew. Sustain. Energy Rev. 91 (2018) 376–393.
[27] H.S. Kim, et al., Relationship between thermoelectric figure of merit and energy conversion efficiency, Proc. Natl. Acad. Sci. USA 112 (27) (2015) 8205–8210.
[28] Y. Yang, et al., Pyroelectric nanogenerators for harvesting thermoelectric energy, Nano Lett. 12 (6) (2012) 2833–2838.
[29] J. Jiang, et al., Giant pyroelectricity in nanomembranes, Nature 607 (7919) (2022) 480.
[30] Y. Zhang, et al., Thermal energy harvesting using pyroelectric-electrochemical coupling in ferroelectric materials, Joule 4 (2) (2020) 301–309.
[31] A. Thakre, et al., Pyroelectric energy conversion and its applicationsflexible energy harvesters and sensors, Sensors 19 (2019) 9.
[32] R. Ghane-Motlagh, et al., A dynamic method for the measurement of pyroelectric properties of materials, Smart Mater. Struct. 27 (2018) 8.
[33] K. Uchino, Electrothermal phenomena in ferroelectrics, Actuators 9 (2020) 4.
[34] S.B. Lang, Sourcebook of pyroelectricity. Ferroelectrics and Related Phenomena, Gordon and Breach Science Publishers, London, New York, 1974 xv, 562 p.

[35] P. Muralt, Micromachined infrared detectors based on pyroelectric thin films, Rep. Prog. Phys. 64 (10) (2001) 1339–1388.
[36] R.L. Byer, C.B. Roundy, Pyroelectric Coefficient Direct Measurement Technique And Application To A Nsec Response Time Detector, Ferroelectrics 3 (2–3-) (1972) 333. -&.
[37] A. Chynoweth, Dynamic method for measuring the pyroelectric effect with special reference to barium titanate, J. Appl. Phys. 27 (1) (1956) 78–84.
[38] M.H. You, et al., A self-powered flexible hybrid piezoelectric-pyroelectric nanogenerator based on non-woven nanofiber membranes, J. Mater. Chem. A 6 (8) (2018) 3500–3509.
[39] S. Patel, A. Chauhan, R. Vaish, Large pyroelectric figure of merits for Sr-modified $Ba_{0.85}Ca_{0.15}Zr_{0.1}Ti_{0.9}O_3$ ceramics, Solid State Sci. 52 (2016) 10–18.
[40] Q. Zhang, R.W. Whatmore, Improved ferroelectric and pyroelectric properties in Mn-doped lead zirconate titanate thin films, J. Appl. Phys. 94 (8) (2003) 5228–5233.
[41] A. Thakre, et al., Enhancement of pyroelectricity in Mn-doped (011) 71Pb($Mg_{1/3}Nb_{2/3}$)O_3-6PbZrO_3-23PbTiO_3 single crystals, Appl. Phys. Lett. 119 (2021) 15.
[42] A.M. Balakt, C.P. Shaw, Q. Zhang, Giant pyroelectric properties in La and Ta co-doped lead-free 0.94$Na_{0.5}Bi_{0.5}TiO_3$-0.06BaTiO_3 ceramics, J. Alloy. Compd. 709 (2017) 82–91.
[43] N.C.T. Ngo, et al., Enhancing low-grade waste heat recovery by lead-free ferroelectric Ba($Zr_{0.1}Ti_{0.9}$)O_3 with Sr and Ca isovalent dopants, Ceram. Int. 49 (10) (2023) 16290–16296.
[44] K.S. Srikanth, et al., Pyroelectric signals in (Ba,Ca)TiO_3-xBa(Sn,Ti)O-$_3$ ceramics: a viable alternative for lead-based ceramics, Scr. Mater. 146 (2018) 146–149.
[45] Q.P. Wang, et al., Effect of Zr/Ti ratio on microstructure and electrical properties of pyroelectric ceramics for energy harvesting applications, J. Alloy. Compd. 710 (2017) 869–874.
[46] A. Thakre, et al., Enhanced pyroelectric response from domain-engineered lead-free ($K_{0.5}Bi_{0.5}TiO_3$-BaTiO_3)-$Na_{0.5}Bi_{0.5}TiO_3$ ferroelectric ceramics, J. Eur. Ceram. Soc. 41 (4) (2021) 2524–2532.
[47] S.L. Jiang, et al., Enhanced pyroelectric properties of porous $Ba_{0.67}Sr_{0.33}TiO_3$ ceramics fabricated with carbon nanotubes, J. Alloy. Compd. 636 (2015) 93–96.
[48] H.B. Zhang, S.L. Jiang, K. Kajiyoshi, Enhanced pyroelectric and piezoelectric figure of merit of porous $Bi_{0.5}(Na_{0.82}K_{0.18})_{0.5}TiO_3$ lead-free ferroelectric thick films, J. Am. Ceram. Soc. 93 (7) (2010) 1957–1964.
[49] K.S. Srikanth, V.P. Singh, R. Vaish, Enhanced pyroelectric figure of merits of porous $BaSn_{0.05}Ti_{0.95}O_3$ ceramics, J. Eur. Ceram. Soc. 37 (13) (2017) 3943–3950.
[50] R.B. Sun, et al., Pyroelectric properties of Mn-doped 94.6$Na_{0.5}Bi_{0.5}TiO_3$-5.4BaTiO_3 lead-free single crystals, J. Appl. Phys. 115 (2014) 7.
[51] S.B. Lang, D.K. Das-Gupta, Pyroelectricity: Fundamentals and applications. Handbook of advanced electronic and photonic materials and devices, Elsevier, 2001, pp. 1–55.
[52] L.W. Hu, et al., Enhanced pyroelectric properties of BNT-xBNN lead-free ferroelectric ceramics for energy harvesting, J. Alloy. Compd. (2023) **948**.
[53] X.Y. Lei, et al., Dielectric and enhanced pyroelectric properties of ($Pb_{0.325}Sr_{0.675}$) TiO3 ceramics under direct current bias field, Appl. Phys. Lett. 101 (26) (2012).
[54] J.A. Gallagher, J. Tian, C.S. Lynch, Composition dependence of field induced phase transformations in [011](C) PIN-PMN-PT relaxor ferroelectric single crystals with d(322) piezoelectric mode, Acta Mater. 81 (2014) 512–523.
[55] F.A. He, et al., Preparation of organosilicate/PVDF composites with enhanced piezoelectricity and pyroelectricity by stretching, Compos. Sci. Technol. 137 (2016) 138–147.
[56] A. Hussain, et al., Synthesis of 0.64 Pb ($Mg_{1/3}Nb_{2/3}$) O_3–0.36 PbTiO_3 ceramic near morphotropic phase boundary for high performance piezoelectric, ferroelectric and pyroelectric applications, J. Asian Ceram. Soc. 4 (3) (2016) 337–343.
[57] T. Yu, et al., Pyroelectric energy harvesting devices based-on Pb[(Mn_xNb_{1-x})$_{1/2}$(Mn_xSb_{1-x})$_{1/2}$]$_y$(Zr_zTi_{1-z})$_{1-y}O_3$ ceramics, Sens. Actuators a-Phys. 223 (2015) 159–166.
[58] Z.N. Wang, et al., Light-induced pyroelectric effect as an effective approach for ultrafast ultraviolet nanosensing, Nat. Commun. (2015) **6**.
[59] J.W. Stewart, et al., Ultrafast pyroelectric photodetection with on-chip spectral filters, Nat. Mater. 19 (2) (2020) 158.
[60] P. Costa, et al., Recent progress on piezoelectric, pyroelectric, and magnetoelectric polymer-based energy-harvesting devices. Energy Technol. 7 (2019) 7.
[61] W. Clingman, R. Moore Jr, Application of ferroelectricity to energy conversion processes, J. Appl. Phys. 32 (4) (1961) 675–681.
[62] J. Childress, Application of a ferroelectric material in an energy conversion device, J. Appl. Phys. 33 (5) (1962) 1793–1798.
[63] Drummond, J. Dielectric power conversion. in Energy 10; Annual Intersociety Energy Conversion and Engineering Conference. 1975.
[64] R.B. Olsen, Ferroelectric conversion of heat to electrical EnergyA demonstration, J. Energy 6 (2) (1982) 91–95.
[65] I.M. McKinley, R. Kandilian, L. Pilon, Waste heat energy harvesting using the Olsen cycle on 0.945Pb($Zn_{1/3}Nb_{2/3}$)O_3-0.055PbTiO_3 single crystals, Smart Mater. Struct. 21 (2012) 3.
[66] A. Navid, L. Pilon, Pyroelectric energy harvesting using Olsen cycles in purified and porous poly(vinylidene fluoride-trifluoroethylene) [P(VDF-TrFE)] thin films, Smart Mater. Struct. 20 (2011) 2.
[67] F.Y. Lee, et al., Pyroelectric energy conversion using PLZT ceramics and the ferroelectric-ergodic relaxor phase transition. Smart, Mater. Struct. 22 (2013) 2.
[68] G. Sebald, S. Pruvost, D. Guyomar, Energy harvesting based on Ericsson pyroelectric cycles in a relaxor ferroelectric ceramic. Smart, Mater. Struct. 17 (2008) 1.
[69] B. Bhatia, et al., High power density pyroelectric energy conversion in nanometer-thick $BaTiO_3$ films, Nanoscale Microsc. Thermophys. Eng. 20 (3–4) (2016) 137–146.
[70] R.B. Olsen, D.A. Bruno, J.M. Briscoe, Pyroelectric conversion cycles, J. Appl. Phys. 58 (12) (1985) 4709–4716.
[71] G. Cha, Y.S. Ju, Pyroelectric energy harvesting using liquid-based switchable thermal interfaces, Sens. Actuators a-Phys. 189 (2013) 100–107.
[72] H. Nguyen, A. Navid, L. Pilon, Pyroelectric energy converter using co-polymer P (VDF-TrFE) and Olsen cycle for waste heat energy harvesting, Appl. Therm. Eng. 30 (14–15) (2010) 2127–2137.
[73] J. Kim, et al., Pyroelectric power generation from the waste heat of automotive exhaust gas, Sustain. Energy Fuels 4 (3) (2020) 1143–1149.
[74] S. Pandya, et al., *New approach to waste-heat energy harvesting: pyroelectric energy conversion.* Npg Asia, Materials (2019) **11**.
[75] B. Bhatia, et al., High-frequency thermal-electrical cycles for pyroelectric energy conversion, J. Appl. Phys. 116 (2014) 19.
[76] M.H. Park, et al., Toward a multifunctional monolithic device based on pyroelectricity and the electrocaloric effect of thin antiferroelectric $Hf_xZr_{1-x}O_2$ films, Nano Energy 12 (2015) 131–140.
[77] Y. Chen, et al., A flexible PMN-PT ribbon-based piezoelectric-pyroelectric hybrid generator for human-activity energy harvesting and monitoring, Adv. Electron. Mater. 3 (2017) 3.
[78] T.T. Zhao, et al., Flexible pyroelectric device for scavenging thermal energy from chemical process and as self-powered temperature monitor, Appl. Energy 195 (2017) 754–760.
[79] M. Fattori, et al., A printed proximity-sensing surface based on organic pyroelectric sensors and organic thin-film transistor electronics, Nat. Electron. 5 (5) (2022) 289–299.
[80] J. Lee, et al., Enhanced pyroelectric conversion of thermal radiation energy: energy harvesting and non-contact proximity sensor, Nano Energy (2022) **97**.
[81] J.H. Lee, et al., Highly stretchable piezoelectric-pyroelectric hybrid nanogenerator. Adv. Mater. 26 (5) (2014) 765–769.
[82] Y. Yang, et al., Flexible hybrid energy cell for simultaneously harvesting thermal, mechanical, and solar energies, ACS Nano 7 (1) (2013) 785–790.
[83] H.S. Choi, et al., Continuous pyroelectric energy generation with cyclic magnetic phase transition for low-grade thermal energy harvesting, Appl. Energy 344 (2023) 121271.
[84] N. Saurabh, R. Kiran, S. Patel, Solar energy harvesting using lead-free pyroelectric bulk ceramICS: A SIMUlation study, J. Sci.: Adv. Mater. Devices 8 (1) (2023), 100527.
[85] H. Wang, et al., Achieving milliwatt level solar-to-pyroelectric energy harvesting via simultaneous boost to photothermal conversion and thermal diffusivity, Nano Energy (2023), 108184.
[86] M. Sharma, et al., Pyroelectric materials for solar energy harvesting: a comparative study, Smart Mater. Struct. 24 (2015) 10.
[87] M.Y. Xie, et al., Wind-driven pyroelectric energy harvesting device, Smart Mater. Struct. 25 (2016) 12.
[88] Tesla, N., Pyromagneto-electric generator. 1890: US428057.
[89] Tesla, N., Thermo-magnetic motor. 1889: US396121.
[90] Thomas, E., Pyromagnetic generator. 1892: US476983.
[91] Thomas, E., Pyromagnetic motor. 1888: US380100.
[92] C. Jiang, et al., Numerical and experimental investigations on a regenerative static thermomagnetic generator for low-grade thermal energy recovery, Appl. Energy (2022) **311**.
[93] M. Ujihara, G.P. Carman, D.G. Lee, Thermal energy harvesting device using ferromagnetic materials, Appl. Phys. Lett. 91 (2007) 9.
[94] D. Dzekan, et al., Efficient and affordable thermomagnetic materials for harvesting low grade waste heat, APL Mater. 9 (1) (2021), 011105.
[95] C.J. Hsu, et al., Thermomagnetic conversion efficiencies for ferromagnetic materials, J. Appl. Phys. 110 (2011) 12.
[96] X. Liu, et al., Significant optimization of active thermomagnetic generator for low-grade waste heat recovery, Appl. Therm. Eng. 221 (2023), 119827.
[97] A. Waske, et al., Energy harvesting near room temperature using a thermomagnetic generator with a pretzel-like magnetic flux topology, Nat. Energy 4 (1) (2019) 68–74.
[98] Y.X. Wang, et al., Outstanding comprehensive performance of La(Fe, Si)(13)H-y/In composite with durable service life for magnetic refrigeration, Adv. Electron. Mater. 4 (2018) 5.
[99] Z.H. Ma, et al., Thermomagnetic generation performance of Gd and La(Fe, $Si)_{13}H_y$/In material for low-grade waste heat recovery, Adv. Sustain. Syst. 5 (2021) 3.
[100] J. Joseph, et al., Upscaling of thermomagnetic generators based on heusler alloy films, Joule 4 (12) (2020) 2718–2732.
[101] R.A. Kishore, et al., Energy scavenging from ultra-low temperature gradients, Energy Environ. Sci. 12 (3) (2019) 1008–1018.
[102] J.S. Chun, et al., Thermo-magneto-electric generator arrays for active heat recovery system, Sci. Rep. (2017) **7**.
[103] H.-C. Song, et al., Modulated magneto-thermal response of $La_{0.85}Sr_{0.15}MnO_3$ and ($Ni_{0.6}Cu_{0.2}Zn_{0.2}$)Fe_2O_4 composites for thermal energy harvesters, Energy Harvest. Syst. 4 (1) (2017) 57–65.
[104] J.S. Chun, et al., Self-powered temperature-mapping sensors based on thermo-magneto-electric generator, Acs Appl. Mater. Interfaces 10 (13) (2018) 10796–10803.
[105] R. Ahmed, et al., Power generation by a thermomagnetic engine by hybrid operation of an electromagnetic generator and a triboelectric nanogenerator, Int. J. Energy Res. 43 (11) (2019) 5852–5863.

[106] C. Rodrigues, et al., Hybridizing triboelectric and thermomagnetic effects: a novel low-grade thermal energy harvesting technology, Adv. Funct. Mater. 32 (2022) 21.
[107] X.L. Cao, et al., Thermal-mechanical-electrical energy conversion system based on Curie effect and soft-contact rotary triboelectric nanogenerator, Nano Research (2022).
[108] R. Zito Jr, Thermogalvanic energy conversion, AIAA J. 1 (9) (1963) 2133–2138.
[109] R. Chasmar, R. Stratton, The thermoelectric figure of merit and its relation to thermoelectric generators, Int. J. Electron. 7 (1) (1959) 52–72.
[110] C.T. Gao, S.W. Lee, Y. Yang, Thermally regenerative electrochemical cycle for low-grade heat harvesting, Acs Energy Lett. 2 (10) (2017) 2326–2334.
[111] J.J. Wang, et al., "Thermal charging" phenomenon in electrical double layer capacitors, Nano Lett. 15 (9) (2015) 5784–5790.
[112] P.A. Linford, Lithium ion power generator: a novel system for direct thermal to electric energy conversion, Massachusetts Institute of Technology, 2017.
[113] M.J. Schmid, et al., Concentration effects on the entropy of electrochemical lithium deposition: implications for Li+ solvation, J. Phys. Chem. B 119 (42) (2015) 13385–13390.
[114] N.P. Yao, L.A. Heredy, R.C. Saunders, Emf measurements of electrochemically prepared lithium-aluminum alloy, J. Electrochem. Soc. 118 (7) (1971) 1039. &.
[115] Y. Reynier, et al., Entropy of Li intercalation in Li_xCoO_2, Phys. Rev. B 70 (17) (2004), 174304.
[116] J.P. Pereiraramos, et al., A thermodynamic study of electrochemical lithium insertion into vanadium pentoxide, Electrochim. Acta 33 (7) (1988) 1003–1008.
[117] M. Bonetti, et al., Huge Seebeck coefficients in nonaqueous electrolytes, J. Chem. Phys. 134 (2011) 11.
[118] A. Gunawan, et al., Liquid thermoelectrics: review of recent and limited new data of thermogalvanic cell experiments, Nanoscale Microsc. Thermophys. Eng. 17 (4) (2013) 304–323.
[119] J.J. Duan, et al., Aqueous thermogalvanic cells with a high Seebeck coefficient for low-grade heat harvest, Nat. Commun. (2018) 9.
[120] B.Y. Yu, et al., Thermosensitive crystallization-boosted liquid thermocells for low-grade heat harvesting, Science 370 (6514) (2020) 342.
[121] Y. Han, et al., High-thermopower polarized electrolytes enabled by methylcellulose for low-grade heat harvesting, Sci. Adv. 8 (7) (2022) eabl5318.
[122] C.-G. Han, et al., Giant thermopower of ionic gelatin near room temperature, Science 368 (6495) (2020) 1091–1098.
[123] P.A. Linford, et al., Multi-cell thermogalvanic systems for harvesting energy from cyclic temperature changes, J. Power Sources 399 (2018) 429–435.
[124] A.D. Poletayev, et al., Continuous electrochemical heat engines, Energy Environ. Sci. 11 (10) (2018) 2964–2971.
[125] D. Zhang, et al., Stretchable thermogalvanic hydrogel thermocell with record-high specific output power density enabled by ion-induced crystallization, Energy Environ. Sci. 15 (7) (2022) 2974–2982.
[126] C.R. Bowen, et al., A modified figure of merit for pyroelectric energy harvesting, Mater. Lett. 138 (2015) 243–246.
[127] M. Sharma, R. Vaish, V.S. Chauhan, Development of figures of merit for pyroelectric energy-harvesting devices, Energy Technol. 4 (7) (2016) 843–850.
[128] G. Sebald, E. Lefeuvre, D. Guyomar, Pyroelectric energy conversion: optimization principles, Ieee Trans. Ultrason. Ferroelectr. Freq. Control 55 (3) (2008) 538–551.

Dr. Sunghoon Hur is a senior research scientist in Korea Institute of Science and Technology (KIST) after joined in 2020. He received his Ph.D. from University of Michigan, Ann Arbor in 2019. His research interest is focused on the energy-conversion materials characterization and property measurements. Specifically, understanding the correlation between electrical, thermal and mechanical stimulus in materials is of interest.

Dr. Sangtae Kim is an assistant professor in Department of Nuclear Engineering, Hanyang University, Seoul. He received his Ph.D. in materials science from Massachusetts Institute of Technology with a thesis titled 'Electrochemically driven Mechanical Energy Harvesting.' He joined Korea Institute of Science and Technology since receiving his Ph.D. and worked on electro-chemo-mechanical behavior and applications of piezoelectric materials.

Prof. Tae-Hyun Sung holds a B.A. (1982), an M.S. (1987) in inorganic material engineering from Hanyang University and a Ph.D. (1991) in Material Science and Engineering from Tokyo Institute of Technology. Professor Sung worked at International Superconductivity Technology Center (ISTEC) as a researcher (1992). He was in Massachusetts Institute of Technology (MIT) as a Post doc. (1995). Before joining the Hanyang faculty in 2009, Professor Sung worked at the Korea Electric Power Research Institute (KEPRI) as a group leader of superconductivity group. His research interests include superconductivity, electrical material, energy storage device and piezoelectric energy harvesting technology.

Prof. Jungho Ryu received his Ph.D. in materials science and engineering at Seoul National University, Korea in 2001. During his Ph.D. and later in his post-doctoral tenure (2001–2003), he had studied magnetoelectric composites and piezoelectric materials at the Pennsylvania State University, USA. Prior to joining Yeungnam University in 2018, he was a senior engineer and project leader at Samsung Electro-Mechanics Co. Ltd, Korea (2003–2006) and a principal researcher at Korea Institute of Materials Science (KIMS), Korea (2006–2018). His current research interests include the development of piezoelectric and ferroelectric devices, energy harvesting, and functional thin/thick ceramic films.

Dr. Jeong Min Baik is Professor in School of Advanced Materials Science and Engineering, Sungkyunkwan University (SKKU). He received his Ph.D. from Pohang University in Department of Materials Science and Engineering in 2006. His recent research interest is focused on the synthesis of nanomaterials and nanostructures such as nanoparticles, nanowires, nanolayers, and nanopores for the applications of Energy-Conversion Devices and Nano-photonic Devices. Particular interests are concerned with the development of Piezoelectric/Triboelectric Nanogenerators and Artificial Photosynthesis.

Dr. Hyun-Cheol Song is a principal research scientist in Korea Institute of Science and Technology (KIST) after joined in 2006. He received the B.S. and M.S. degree in Materials Science and Engineering from Korea University, 2004 and 2006, respectively. In 2017, he received Ph.D. in the same field from Virginia Tech. His research interests are now on, piezoelectric and triboelectric energy harvesting, MEMS devices, nanostructured piezoelectric materials, textured piezoelectric ceramics, piezocatalyst, and magneto-thermoelectric generators.